

2023

# Characterization of synaptic connections in the thalamic reticular nucleus of primates

---

<https://hdl.handle.net/2144/46422>

*"Downloaded from OpenBU. Boston University's institutional repository."*

BOSTON UNIVERSITY  
SARGENT COLLEGE OF HEALTH AND REHABILITATION SCIENCES

Thesis

**CHARACTERIZATION OF SYNAPTIC CONNECTIONS IN THE  
THALAMIC RETICULAR NUCLEUS OF PRIMATES**

by

**REBECCA JOHNSON**

B.S., Boston University, 2022

Submitted in partial fulfillment of the  
requirements for the degree of  
Master of Science

2023

© 2023 by  
REBECCA JOHNSON  
All rights reserved

Approved by

First Reader

---

Vasileios Zikopoulos, Ph.D.  
Associate Professor of Human Physiology  
Boston University, Sargent College of Health and Rehabilitation  
Sciences

Associate Professor of Anatomy & Neurobiology  
Boston University, Chobanian & Avedisian School of Medicine

Second Reader

---

Xuefeng Liu, Ph.D.  
Senior Post-Doctoral Fellow

## **ACKNOWLEDGMENTS**

I want to thank everyone I met and had the opportunity to work with during my time in the Human Systems lab. Each of you played an important part in solidifying my interest in neuroscience research, and I couldn't be more grateful for this experience. Of these people, I would specifically like to thank Xuefeng Liu for teaching me the foundational techniques of this research and for offering his encouragement throughout the process. And of course, a big thank you to my wonderful thesis advisor, Basilis Zikopoulos, who let me into his lab and taught me all I know about the TRN.

**CHARACTERIZATION OF SYNAPTIC CONNECTIONS IN THE  
THALAMIC RETICULAR NUCLEUS OF PRIMATES**

**REBECCA JOHNSON**

**ABSTRACT**

Communication between the cortex and thalamus is imperative for performing cognitive processes. This communication can be modulated at the level of the thalamus through a strategically positioned inhibitory nucleus called the thalamic reticular nucleus (TRN). The TRN's ability to modify thalamocortical communication through a distinctly inhibitory action has implicated it in the sleep-wake cycle and in selective attention, where its effects are so profound that it has commonly been coined the attentional searchlight of the brain. While the TRN projects to the thalamus only, it receives input from both cortical and thalamic projections which organize topographically into sectors within the TRN. These projections can either be categorized as core or matrix, which refer to first-order sensory or high-order association, respectively. The topographic organization of these two projection types into sectors within the TRN creates functional diversity, as well as complexity. Neuroscientists have begun to consider the importance of core-matrix fibers as their integration is central to the brain's ability to perform complex and dynamic functions. However, little is known about the organizational aspects underlying their divergent sensory and association functions which is central to further classifying the broad functions of thalamocortical communication. Additionally, disruptions in circuitry at the level of the TRN can act as a precursor to numerous neurological deficits and disease, which further stresses a need for a morphological

understanding of these functionally distinct regions. To address this gap in knowledge, we examined functionally distinct regions on the basis of their core-matrix distributions and compared their morphological features through the use of electron microscopy (EM) and brightfield microscopy (BF). We hypothesize that there will be cellular and dendritic architectural differences in regions with core and matrix distinctions, confirming that TRN sectors are heterogenous not just on a functional basis but also on an anatomic basis. In regions predominated with matrix projections, synaptic density was shown to be preserved across dendritic order while bouton diameters decreased across all orders of dendrites. Meanwhile, for regions populated with core fibers, synaptic density decreased between some orders of dendrites, and bouton diameter was mostly preserved across all orders of dendrites. Furthermore, across the TRN as a whole, the vast majority of boutons were deemed to be excitatory. The relative proportions of boutons arising from other brain afferents such as the amygdala, superior colliculus, and basal ganglia were different among the sectors predominated with core and matrix fibers, suggesting a specific balance of excitation and inhibition is required for TRN function. As such, heterogeneity was confirmed in the TRN on a morphological basis.

## TABLE OF CONTENTS

ACKNOWLEDGMENTS .....	iv
ABSTRACT.....	v
TABLE OF CONTENTS.....	vii
LIST OF TABLES .....	x
LIST OF FIGURES .....	xi
LIST OF ABBREVIATIONS.....	xii
1. INTRODUCTION .....	1
1.1 Thalamocortical communication .....	1
1.2 TRN organization and function in thalamocortical communication.....	2
1.2.1 The TRN's role in thalamocortical modulation.....	2
1.2.2 TRN topography .....	3
1.3 Other TRN afferents .....	4
1.3.1 Amygdala.....	4
1.3.2 Basal ganglia.....	5
1.3.3 Brainstem and basal forebrain .....	5
1.4 TRN structure and morphology .....	8
1.4.1 TRN anatomy and neurochemical properties .....	8
1.4.2 Cellular and dendritic architecture.....	9
1.4.3 TRN synapses .....	10
1.5 Aims.....	13

2. METHODS .....	14
2.1 Experimental approach .....	14
2.2 Tissue selection.....	16
2.3 Tissue origin .....	18
2.4 Surgical procedures.....	19
2.5 Perfusion procedures.....	19
2.6 Immunohistochemical experiments .....	20
2.6.1 Brightfield staining .....	20
2.6.2 Electron microscopy .....	21
2.7 Imaging .....	22
2.7.1 Brightfield microscopy .....	22
2.7.2 Electron microscopy .....	25
2.8 Analysis .....	26
2.8.1 Brightfield analysis .....	26
2.8.2 EM analysis.....	28
2.8.3 Bouton analysis.....	30
2.9 Statistics .....	31
3. RESULTS .....	32
3.1 Dendritic branching and categorization of dendritic order.....	32
3.2 Soma analysis .....	40
3.3 Synaptic density .....	40
3.4 Characterizing the bouton: Size, shape, mitochondria, and origin .....	45

3.4.1 Size.....	45
3.4.2 Shape.....	48
3.4.3 Mitochondria and Origin.....	50
3.5 Fillopodia and Spines.....	57
4. DISCUSSION.....	59
4.1 Limitations and future analyses .....	63
5. CONCLUSION.....	65
BIBLIOGRAPHY.....	66
CURRICULUM VITAE.....	73

## LIST OF TABLES

Table 1. Bouton Categories.....	12
Table 2. Experimental Record .....	18
Table 3. Electron Microscopy Sampling .....	29
Table 4. Bouton Sampling .....	31

## LIST OF FIGURES

Figure 1. Topography and Afferents of the TRN .....	7
Figure 2. Experimental Approach.....	17
Figure 3. Brightfield Microscopy Image Acquisition.....	24
Figure 4. Sampling and Classification of Dendritic Order .....	27
Figure 5. 3D Reconstructions of Synapses in the TRN .....	30
Figure 6. Thickness of Dendrites Across Dendritic Order. ....	33
Figure 7. Average Dendritic Thickness in the dTRN and vTRN .....	34
Figure 8. 3D Reconstruction of Dendritic Branching from Electron Microscopy .....	36
Figure 9. Dendritic Order Clustering of Electron Microscopy .....	39
Figure 10. Synaptic Density in the dTRN and vTRN.....	43
Figure 11. Dendritic Thickness and Synaptic Density.....	44
Figure 12. Characterization of Bouton Size.....	47
Figure 13. Characterizing Bouton Shape and Size .....	49
Figure 14. Relative Abundance of Bouton Classes .....	53
Figure 15. Electron Microscopy Bouton Categories.....	55
Figure 16. Filopodia and Thorns Visualized by EM.....	58
Figure 17. Summary of Synapse Distributions.....	62

## LIST OF ABBREVIATIONS

AB	Avidin-biotin
ADT	Average Dendritic Thickness
ANOVA	Analysis of Variance
BF	Brightfield
BG	Basal ganglia
CB	Calbindin
CR	Calretinin
DAB	3, 3'-diaminobenzidine
dTRN	Dorsal thalamic reticular nucleus
EM	Electron microscopy
GABA	Gamma aminobutyric acid
GPe	Globus pallidus externus
HRP	Horseradish peroxidase
K-S	Kolmogorov-Smirnov
LGN	Lateral geniculate nucleus
MD	Mediodorsal nucleus
MRI	Magnetic resonance imaging
PB	Phosphate buffer
PBS	Sodium phosphate buffer
PSD	Post-synaptic density
PV	Parvalbumin

ROI	Region of interest
SC	Superior colliculus
SD	Synaptic density
SMI-32	Monoclonal antibody to neurofilament protein
SNr	Substantia nigra pars reticulata
TRN	Thalamic reticular nucleus
vTRN	Ventral thalamic reticular nucleus

# 1. INTRODUCTION

## 1.1 Thalamocortical communication

The thalamus and cortex have critical connectivity for mediating the functions of everyday living such as consciousness, cognition, sleep, and attention (Zikopoulos and Barbas, 2007a; Zikopoulos and Barbas, 2007b). Deficits in such connectivity is the hallmark of numerous neurological and psychiatric diseases (Llinás and Steriade, 2006; Kong et al., 2018, Jiang et al., 2021). Reciprocal circuits between the dorsal thalamus and cortex rely on two kinds of thalamic nuclei: first-order sensory thalamic nuclei, also called “core” nuclei, which perform thalamocortical communication by relaying information from ascending pathways to specific cortical regions, and higher-order association thalamic nuclei, also called “matrix” nuclei, that play a role in corticocortical communication by which processed cortical information is projected broadly to numerous cortical regions (Guillery, 1995; Sherman and Guillery, 2002; Zikopoulos and Barbas, 2007b). As such, relays to primary sensory areas are mostly first-order while relays to other cortical regions are mostly high-order but may also exist as a mixture of both (Sherman and Guillery, 2002). Relevant to core and matrix circuits is the idea of “drivers” and “modulators,” a concept first introduced in sensory systems. Drivers ensure the transmission of signals while modulators modify the signal without interfering with foundational receptive field properties (Sherman and Guillery, 2002). First order nuclei receive modulatory input from pyramidal cells in cortical layer VI and send projections to layer IV while higher order nuclei receive modulatory input primarily from cortical layer

V and send projections to layer I (Guillery, 1995; Bickford, 2016). Importantly, most afferents in the cortex are modulators, as only 5–10% of synapses from genicular afferents make up the driving input (Sherman and Guillery, 2002).

## **1.2 TRN organization and function in thalamocortical communication**

### *1.2.1 The TRN's role in thalamocortical modulation*

Arising embryologically from the ventral thalamus and strategically positioned between the dorsal thalamus and cortex to intercept and modulate thalamocortical communication is the TRN, a thin umbrella-shaped meshwork of inhibitory neurons that encapsulates the entire anteroposterior thalamus in primates (Pinault, 2004; Zikopoulos and Barbas, 2006). Thalamocortical and corticothalamic fibers pass through the TRN, giving the nucleus its' notable reticulated appearance. As such, the TRN receives unidirectional projections from the cortex and has reciprocal connectivity with thalamic nuclei (Zikopoulos and Barbas, 2006). Identified from electrophysiological studies, projections from the cortex or thalamic nuclei provide excitatory input to the TRN while the TRN exerts a distinct inhibitory action on the dorsal thalamic nuclei (Ohara and Lieberman, 1985; Pinault, 2004; Zikopoulos and Barbas, 2007a). Due to its role in the modulation of thalamocortical neuronal firing patterns through an inhibitory action on the thalamus, the TRN is thought to be implicated in the transition from wakefulness to sleep and has been coined the attentional searchlight due to its' presumed role in selective attention, or the ability to focus on a task in a stimulus or distraction-rich environment (Francis Crick, 1984; Pinault, 2004; Zikopoulos and Barbas, 2007a; Crabtree, 2018).

### *1.2.2 TRN topography*

First outlined by Jones in a comprehensive cross-species study that utilized anterograde and retrograde tracers, the TRN was identified as containing overlapping sectors correlated to specific dorsal thalamic nuclei. Thalamocortical and corticothalamic fibers project to and from thalamic nuclei and then terminate in the TRN sectors associated with that given nucleus. In return, the cells from these TRN sectors send their axons to the dorsal thalamic nuclei they are related to as indicated by the corresponding corticothalamic and thalamocortical fibers (Jones, 1975, 1985). As previously discussed, these thalamic nuclei may be first- or higher-order and send projections corresponding to these classifications, creating topography in the TRN on the basis of their core-matrix distributions as well. The result of this organization is the formation of heterogeneous topographic zones with varying functionalities (Lubke, 1993; Crabtree, 1998; Zikopoulos and Barbas, 2007a). In fact, given that these sectors have unique anatomy defined by the afferent and efferent fiber patterns and their associated first-order and higher-order thalamic nuclei, the TRN has significant diversity in function and is thought to encode for almost all functional modalities (Pinault, 2004; Berezhnaya, 2006). Specifically, five sensory (somatosensory, auditory, visual, visceral, and gustatory), one motor, and one limbic zone have been shown to exist from studies in rodents. From these, the ventral, anterolateral, dorsocaudal, and ventrocaudal TRN has loosely been associated with somatosensory, motor, visual, and auditory modalities (Pinault, 2004). However, the boundaries of these sectors are not defined well in primates and are not definite, as

topography may be blurred. For instance, there are regions where sectors overlap more distinctly, adopting a mixed receptive field such as the visual and auditory sectors of the monkey TRN (Jones, 1985; Crabtree, 1996; Zikopoulos and Barbas, 2007a).

### **1.3 Other TRN afferents**

#### *1.3.1 Amygdala*

As aforementioned, the TRN's interactions with the thalamus are important for the mediation of selective attention (Lubke, 1993; Zikopoulos and Barbas, 2007a). Recently, a novel pathway thought to mediate selective attention in the context of emotions in primates was identified involving both the TRN and amygdala (Zikopoulos and Barbas, 2012). The amygdala, the brain's emotional system, helps to form long-term associations between various stimuli and their outcomes, transmitting such information to other regions (John et al., 2016). Under exposure to emotionally evoking stimuli, attention is not just shifted toward the stimuli by the amygdala, but it is also actively shifted away from less relevant aspects of the environment, suggesting an additional suppressive effect. Due to the TRN's role in exerting wide inhibitory control to thalamic nuclei as an attentional searchlight, it was suspected to be involved. The robust pathway from the amygdala to the TRN was identified as excitatory, indicating that the brain's emotional system can override that of the profoundly inhibitory attentional system to direct and shift attention (John et al., 2016).

### *1.3.2 Basal ganglia*

The basal ganglia (BG), a set of subcortical nuclei critical for motor control, has been implicated in pathways with the motor TRN (Zikopoulos and Barbas, 2006; Lanciego et al., 2012). Specifically, two of the BG's output nuclei, the globus pallidus externus (GPe) and the substantia nigra pars reticulata (SNr), have been shown to innervate the TRN (Hazrati and Parent, 1991; Gandia et al., 1993; Asanuma, 1994; Tsumori et al., 2002, Guillery and Harting, 2003). The GPe projects abundantly to the TRN with a more widespread distribution and a dorsoventral topographic orientation. Meanwhile, the SNr sends fewer projections and targets the ventral aspect of the TRN primarily in a non-topographic manner (Gandia et al., 1993). The projections sent to the TRN from these output nuclei were also determined to be immunoreactive to GABA ( $\gamma$ -aminobutyric acid), indicating an inhibitory action (Hazrati and Parent, 1991; Gandia et al., 1993; Tsumori et al., 2002). The combined inhibitory nature of the BG and TRN cells suggests that the output nuclei of the BG may be able to disinhibit thalamocortical neurons, influencing thalamocortical communication indirectly (Hazrati and Parent, 1991).

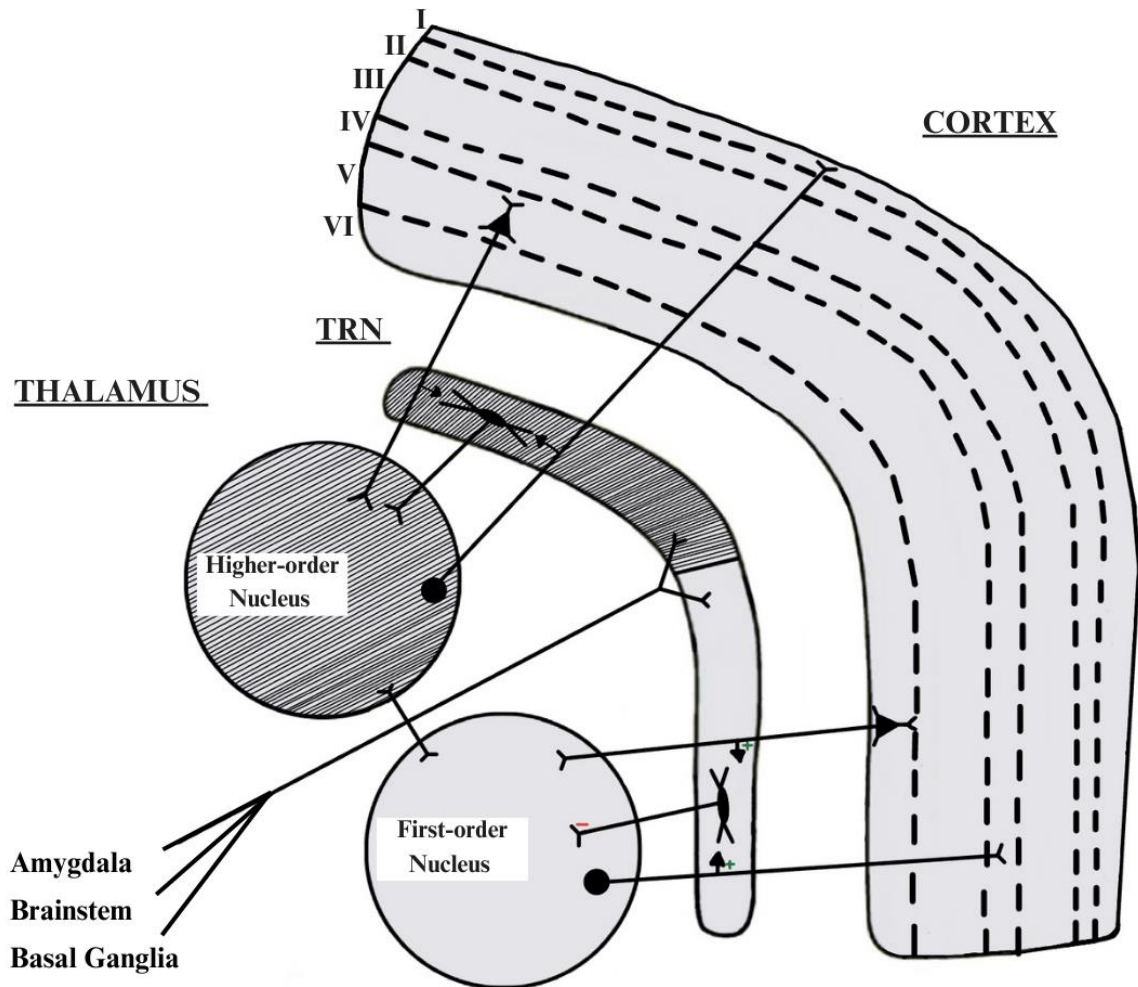
### *1.3.3 Brainstem and basal forebrain*

As briefly mentioned, the TRN is pertinent to the sleep-wake cycle (Marks and Roffwarg, 1993; Zikopoulos and Barbas, 2006). Determined from developmental studies, under the same timeline as the emergence of sleep-wake patterns in the cortex, cholinergic synapses appear in the TRN (Sokhadze et al., 2018a). Importantly, one of the

largest sources of cholinergic input to the TRN arises from the basal forebrain and brainstem. Projections from these areas are extensive and arise from numerous origins (Hallanger et al., 1987; Levey et al., 1987; Asanuma, 1992; Guillery and Harting, 2003). These include the nucleus basalis of the basal forebrain as well as the pedunculopontine and laterodorsal tegmental nuclei of the brainstem. Additionally, other brainstem origins of noncholinergic input to the TRN have been identified such as the serotonergic raphe nucleus and the noradrenergic locus coeruleus (Hallanger et al., 1987; Asanuma, 1992; Rodriguez et al., 2011). Furthermore, the caudal basal forebrain was found to send GABAergic projections to the TRN (Jourdain et al., 1989; Asanuma and Porter, 1990).

Another important brainstem afferent is the superior colliculus (SC), which is responsible for moving the head toward visual stimuli (Basso and May, 2017). Neurons from this region send afferents to thalamic nuclei, specifically those responsible for visual processing, such as the pulvinar nucleus or the lateral geniculate nucleus (LGN) (Jones, 1985). These projections extend beyond the thalamus, as the SC projects directly to the TRN as well, explaining a possible mechanism for how TRN modulates the relay of visual signals to the cortex (Krauzlis et al., 2013). Because of this connectivity, the SC has been implicated in spatial attention. This was identified when monkeys were shown to shift their attention to rapidly fixate on targets in their receptive field through action of the SC, resulting in enhanced visual responses (Basso and May, 2017). The nature of the SC's input is excitatory, which similarly to the amygdala, is likely required to override and shift attention when exposed to stimuli (Crabtree, 2018).

**Figure 1.** Topography and Afferents of the TRN



General organization of the thalamus, cortex, and TRN and their associated projections. Pyramidal cells from layer VI project to first-order thalamic nuclei which send projections to layer IV in return. Meanwhile, pyramidal cells from from layer V send projections to high-order thalamic nuclei which send projections to layer I in return. Corticothalamic and thalamocortical fibers also terminate excitedly in the TRN which then send their own inhibitory projections to the corresponding first- or higher-order thalamic nuclei, creating topography. Note that projections from the thalamus to cortex shown are modulatory. The TRN also receives projections from other brain areas highlighted, including the amygdala, brainstem, and basal ganglia (Adapted from Pinault, 2004; Guillery and Harting, 2003).

## 1.4 TRN structure and morphology

### *1.4.1 TRN anatomy and neurochemical properties*

Aside from being strategically positioned between the thalamus and cortex, it's immediately located laterally to the external medullary lamina and medially to the internal capsule. The primate TRN encapsulates all of the dorsal thalamus and appears as a diencephalic shell, a shape that is relatively conserved across mammals (Jones, 1975; Pinault, 2004). The TRN appears round but begins thinning out rostrally until it elongates and tapers caudally (Zikopoulos and Barbas, 2007a). All the cells in the TRN use GABA as a neurotransmitter, explaining its profound inhibitory effect on thalamic nuclei (Houser et al., 1980). Furthermore, in primates, these neurons tend to be majorly positive for parvalbumin (PV) (~70%), a calcium-binding protein that labels axons from sensory first-order thalamic nuclei that traverse and synapse in the TRN (Zikopoulos and Barbas 2007a). Calcium-binding proteins act as important buffers in the control of cytosolic  $Ca^{2+}$  transients, but also have been identified as a useful tool for labeling topographic distinctions (Pinault, 2004). The distributions of calcium binding proteins, PV, calretinin (CR), and calbindin (CB) within the thalamus suggest neurochemical heterogeneity (Jones, 1998; Munkle et al., 2000; Contreras-Rodriguez et al., 2003). Specifically on the basis of core-matrix distributions, it was indicated that the primate thalamus has a larger population of CB immunoreactivity in matrix nuclei while core nuclei showed a greater population of PV immunoreactivity (Jones 1998; Munkle et al., 2000). Similar trends were shown in thalamocortical pathways coursing through the TRN as the dorsal TRN

(dTRN), which is associated with and receives fibers from the matrix mediodorsal nucleus (MD), is predominated with CB+ axons. Meanwhile, the ventral TRN (vTRN), which is closely associated with and receives projections from the core LGN, showed a prominence of PV+ axons, stressing neurochemical heterogeneity not just in the thalamus but also in the TRN (Pinault 2004; Son, 2022).

#### *1.4.2 Cellular and dendritic architecture*

The TRN contains approximately 1 million neurons distributed on either hemisphere in the adult rhesus brain which have frequently been targeted and categorized based on features such as cellular size, shape, and dendritic arborizations. However, such categorizations are not consistent across all descriptions of TRN morphology as different definitions arise depending on the plane of sectioning as well as the species utilized (Pinault, 2004). Ultimately, much of the data on morphology in the TRN tends to be somewhat controversial. For instance, in rats it was originally postulated that three categories of cellular architecture existed which included small (f) and large fusiform (F) with elongated perikarya or round perikaryon with multipolar dendritic organization (R) (Spreafico, 1988; Spreafico, 1991; Deleuze and Huguenard, 2006). However, this terminology is not used commonly as minimal evidence has been shown for classification of neurons in the TRN according to dendritic morphology (Ohara and Liebermann, 1984; Lubke, 1993; Ohara and Havton, 1996). Despite this, it has been commonly accepted that differences in morphology may be partially explained by the spatial arrangement of TRN cells. Cells that have more space, as they do in the rostral pole of the nucleus, tend to

adopt round perikarya and multipolar dendritic organization, while those limited in space, such as in the central and posterior aspects of the nucleus, tend to have elongated perikarya with flattened dendritic arborizations (Zikopoulos and Barbas, 2007a). Morphological analyses in primates have shown that most neurons have an invaginated nuclear envelope and thin cytoplasm with a fusiform or ovoid shape and diameters of approximately 20-50  $\mu\text{m}$  (Berezhnaya, 2006; Zikopoulos and Barbas, 2007a). In the macaque monkey visual TRN sector, cell body areas ranged from 100–700  $\mu\text{m}^2$  in size with most having areas around 200–300  $\mu\text{m}^2$  (Bragg, 2017). Similar information in other sectors is not widely explored in a primate model. Across species, smooth primary dendrites emerge from somas and branch into long secondary, and shorter distal branches, including the tertiary, quaternary, and quinary branches. TRN dendrites tend to be mostly aspiny; however, at more distal branches, thorns, filipodia, or other hair-like structures may be present (Lubke, 1993).

#### *1.4.3 TRN synapses*

Similar to dendritic morphology, three categories separating boutons based on their features have also been established in a rat model and applied to other species, including the monkey (Ohara, 1988; Williamson, 1993) Specifically, these categories are the D-, L-, and F- terminals (Figure 1) (Ohara, 1988; Williamson et al., 1993; Pinault, 1997; Zikopoulos and Barbas, 2006). The first category, D-terminals, describes boutons arising from the cortex which terminate asymmetrically with a small shape, many spherical vesicles, and usually 0–1 mitochondria. The second category, the L-terminals,

describes boutons arising from the dorsal thalamus which similarly terminate asymmetrically, have spherical vesicles, 2+ mitochondria, and a larger size. Importantly, the boutons in these two categories are glutamatergic and thus excitatory, which can be indicated by their asymmetric terminations. The final category, F-terminals, consists of boutons arising from intrinsic TRN recurrent collaterals or extrinsically from the SNr and GPe of the BG. These boutons tend to have flattened or round vesicles, symmetric synapses, and have GABAergic terminals, indicating an inhibitory action. When differentiating TRN recurrent collaterals and BG structures in this final category, size, mitochondrial content, and synapse location are the most important features to consider. BG boutons tend to terminate more proximally, are larger in size, contain many mitochondria, and have round clear vesicles (Kultas-Ilinsky et al., 1983; Asanuma, 1994). Importantly, through quantitative electron microscopy in the rat, it was determined that on proximal dendrites, 50% of synapses were D-terminal types, 30-40% were L-terminal types, and 10-25% were F-terminal types. Meanwhile, more distally, 60-65% were D-terminal types, 20% were L-terminal types, and 15% were F-terminal types (Liu and Jones, 1999). Thus, this suggests that larger boutons tend to synapse more proximally while smaller boutons tend to synapse more distally (Liu and Jones 1999; Zikopoulos and Barbas, 2007a; Wanaverbecq et al., 2008). It was also noted that very few TRN recurrent collaterals and no dendrodendritic synapses were seen (Liu and Jones, 1999). Breakdowns of terminal percentages in proximal and distal dendrites has not been established recently in primates. Of note, the amygdala or SC were not included in the

original terminal classifications. Amygdala boutons in the TRN are asymmetric, large, and generally synapse on proximal TRN dendrites primarily in the anterior TRN but also in the central and posterior aspects (Zikopoulos and Barbas, 2012; Timbe et al., 2020). Meanwhile, SC boutons in the TRN are also asymmetric, large, and as a result, synapse more proximally in regions closely associated with the thalamic nuclei responsible for visual processing (Partlow et al., 1977). Due to the amygdala and SC's ability to override the TRN for an immediate shift in attention and large bouton size, it suggests an efficiency in activating TRN neurons, which is reflected in high vesicle and mitochondrial content (Zikopoulos and Barbas, 2007a). Aside from these large boutons, there has been evidence showing that amygdala and SC projections may terminate in the same manner as D-terminals (Partlow et al., 1977; Zikopoulos and Barbas, 2012). Without the use of tracers, distinguishing these boutons from those from the cortex would be difficult as they both synapse similarly with comparable vesicular and mitochondrial features.

**Table 1.** Bouton Categories

<b>Action</b>	Excitatory		Inhibitory
<b>Name</b>	D-Terminals*	L-Terminals	F-Terminals
<b>Features</b>	Asymmetric Round vesicles 0-1 Mitochondria	Asymmetric Round vesicles 2+ Mitochondria	Symmetric Flat vesicles
<b>Possible Origin</b>	Cortex	Thalamus Amygdala Superior Colliculus	TRN Recurrent Collaterals Basal Ganglia

\*May have additional origins from amygdala or superior colliculus but cannot differentiate from cortex boutons

## 1.5 Aims

Being initially identified over a century ago, the TRN has been long examined from many lenses; however, much remains elusive. Morphological and topographical studies have implicated the TRN in a wide array of functions and stressed its' importance in gating thalamocortical communication (Ohara and Lieberman, 1985; Spreafico, 1991; Lubke, 1993; Crabtree, 1996; Crabtree, 1998; Berezhnaya, 2006; Bragg, 2017). However, these studies have focused on examinations of the entire TRN or just in individual sectors without a consideration of core-matrix distributions. Thus, little is known about how cellular, dendritic, and synaptic architecture differ in TRN regions populated more by core or matrix circuits. Since topographic and neurochemical heterogeneity has been demonstrated in the TRN, we hypothesize that by leveraging high-resolution EM and BF techniques, heterogeneity on an architectural scale will be observed as well.

Understanding morphological differences in regions predominated with core or matrix fibers may allow for further classification of the broad functions of thalamocortical communication. And since deficits in thalamocortical communication is the hallmark of neurological pathology, characterizing such morphological features may help in formulating a comparative model that could be utilized when attempting to understand the progression of decay and sites of vulnerability in disease.

## 2. METHODS

### 2.1 Experimental approach

From a coronal view, the TRN is closely associated with its' chief MD thalamic nucleus dorsally, thought to be relevant in high-order association functions due to connectivity with the prefrontal cortex. Meanwhile, the ventral aspect is closer to that of the LGN, a thalamic nucleus important for projecting first-order sensory retinal information to the visual cortex (Sherman and Guillery, 2002; Zikopoulos and Barbas, 2006; Weyand, 2015; Ouhaz et al., 2018). As aforementioned and suggested based on their functions, these two nuclei differ, as the MD and LGN nuclei are predominantly matrix and core, respectively. Because of their relative locations to the TRN, the coronal plane provides a valuable view for analyzing differences in morphology as the dTRN represents a matrix sector while the vTRN represents a core sector.

To obtain information relevant for the anatomic and morphological characterization of the TRN, EM and BF techniques were implord (Figure 2A). EM remains the gold standard for analyzing synaptic features such as structure and organization, morphology of thorns, and when immuno-EM is done, details about protein expression in pre- and post-synaptic neurons can be provided (Serrano et al., 2022). Two types of immuno-EM gold labeling were leveraged for EM analysis: GABA in three cases and PV in one case. BF, also referred to as light microscopy, has been a key visualization tool to closely observe cellular features, dendritic branching, and structural organization in the brain (Wilt et al., 2009). BF experiments made use of three antibodies

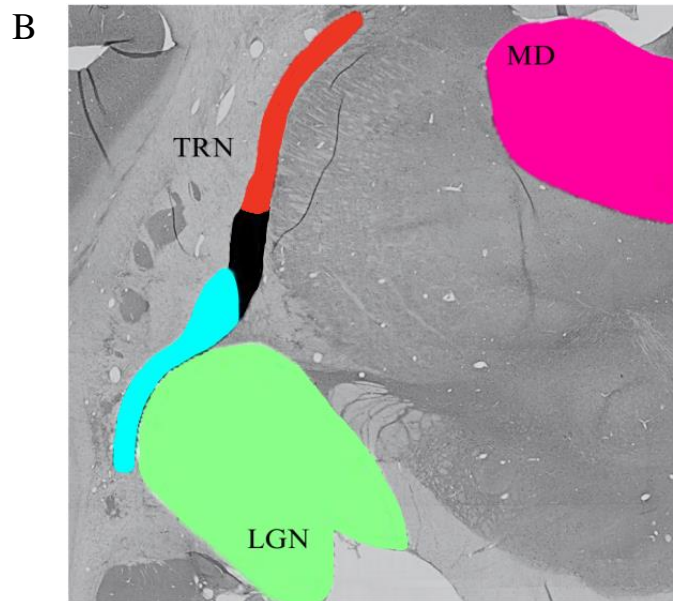
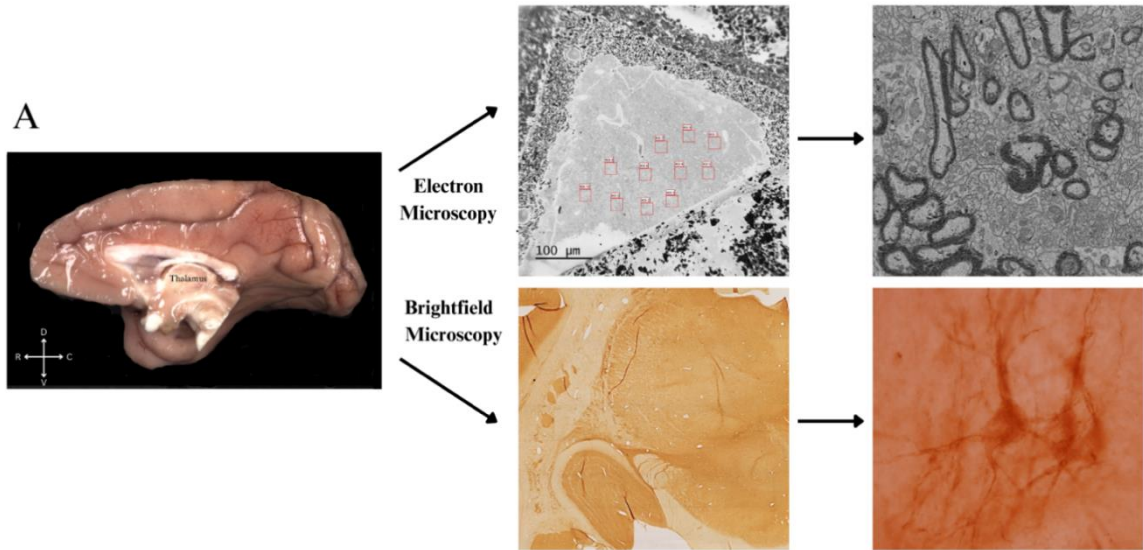
that stained TRN neurons to different extents: PV and CR, which labeled calcium-binding proteins, and SMI-32 which recognized a non-phosphorylated epitope of neurofilament proteins (Campbell and Morrison, 1989; Ouda et al., 2012; Wang and Barbas, 2018). It is important to note that during BF experimentation, some tissues did not receive primary antibody incubation to act as a control. This was deemed successful due to the absence of immunolabeling in such tissues. Both EM and BF techniques were utilized and applied to the dTRN and vTRN to gain a holistic view of morphology by combining small- and large-scale structures.

In our analysis, we first focused on comparing average dendritic thickness (ADT) in the dTRN and vTRN to create categories of dendritic order. Synaptic density (SD), or the bouton count per length of micron, was compared in the dorsal and ventral aspects as well as proximally and distally based on the categories derived from ADT measurements. Furthermore, we examined whether larger dendritic size was correlated with a higher SD and whether larger boutons synapsed with larger dendrites. Then, a categorization of boutons based on the D-, L-, and F- terminal criteria was performed. The percentages of these were compared both dorsally and ventrally as well as proximally and distally. Additional analyses were done examining the relationships between the size of boutons and the mitochondrial content, the size of boutons and their shape, dendritic order and the presence of filopodia or thorns, and the dTRN and vTRN somata areas. Combining all these measurements together served to address whether TRN is heterogenous on a morphological level.

## **2.2 Tissue selection**

Prior to experimentation, tissues were carefully collected to ensure adequate selection for image analyses. Utilizing a rhesus monkey brain atlas, sections containing the high-order and first-order thalamic nuclei involved in thalamocortical pathways, the MD and LGN, were selected (Paxinos et al., 2000). From this, the boundaries of dTRN and vTRN could be determined as they are closely associated with the MD and the LGN, respectively (Figure 2B). Furthermore, dTRN and vTRN aspects can be distinguished on the basis of their neurochemical distributions, as previously described (Son, 2022).

**Figure 2.** Experimental Approach



(A) Tissue processing and image acquisition central to experimental analysis. At the level of MD and LGN, rhesus coronal sections were stained for EM or BF. (B) Differentiation of dTRN and vTRN from SMI-32 BF at 4x magnification. The coronal view was annotated to show important TRN landmarks. The MD nucleus is colored in pink, the LGN in green, and the entire TRN in black. Red and blue outlines overlaying the black tracing represent the dTRN and vTRN, respectively.

### 2.3 Tissue origin

Experiments were conducted on 11 post-mortem rhesus monkeys (*Macaca mulatta*)(Table 2). Tissue was selected from archival tissue provided by the laboratories of Basilis Zikopoulos and Helen Barbas. Guidelines set in place by the National Institutes of Health Guide for the Care and Use of Laboratory Animals were followed during experimentation, and experimental procedures were formulated to ensure minimal animal suffering and population loss. Approval of experimentation was provided by the Institutional Animal Care and Use Committee at Boston University School of Medicine, Harvard Medical School, and New England Primate Research Center (Department of Health, Education, and Welfare Publication no. [NIH] 80-22, revised 1996, Office of Science and Health Report, Division of Receipt and Referral/NIH, Bethesda, MD).

**Table 2.** Experimental Record

Case	Sex	Age	Hemisphere	Experiment	Dorsal or Ventral	Labeling
RBN	M	2 years	Left	EM	Dorsal	GABA
RBQ	F	3.5 years	Right	EM	Dorsal	GABA
RBR	F	3 years	Left	EM	Ventral	PV
RBU	M	4 years	Left	EM	Both	GABA
RBB	F	2 years	Left	BF	Both	SMI-32
RAN	F	2 years	Right	BF	Both	SMI-32
RBC	M	-	Right	BF	Both	PV
RBD	M	2 years	Right	BF	Ventral	PV
RBF	F	-	Left	BF	Dorsal	PV
RAX	F	3 years	Left	BF	Both	CR
RBW	F	5.5 years	Right	BF	Both	CR

Notes: EM, electron microscopy; BF, brightfield microscopy; GABA,  $\gamma$ -aminobutyric acid; PV, parvalbumin; SMI-32, monoclonal antibody to neurofilament protein; CR, calretinin; - , information not documented

## **2.4 Surgical procedures**

As aforementioned, archival tissue which contained injection sites were selected and utilized for experimentation (Wang and Barbas, 2018; Wang et al., 2021). Prior to such injections, Magnetic Resonance Imaging (MRI) was performed to obtain three-dimensional scans of the brains used to calculate of stereotaxic coordinates to maximize tracer potential. To avoid interference, cases with injection sites situated close to the region of interest or utilized incompatible tracers were discarded (Joyce and Barbas, 2018; Wang et al, 2021). One week after the MRI, the monkeys were anesthetized with ketamine hydrochloride (10-15 mg/kg, i.m.) followed by gas anesthetic (isoflurane) until a surgical level of anesthesia was achieved (Wang and Barbas, 2018). The monkeys were then placed in a stereotaxic apparatus, where a small region of the cortex was exposed, allowing for tracer injections to be performed under sterile conditions with constant monitorization of the subject's vitals (respiratory rate, heart rate, oxygen saturation, and temperature).

## **2.5 Perfusion procedures**

Three weeks following tracer injection procedures, the monkeys were anesthetized and given a lethal dose of sodium pentobarbital. Furthermore, depending on the case, they were transcardially perfused with 4% paraformaldehyde and 0.2% glutaraldehyde in 0.1 M phosphate buffer, pH 7.4 or just 4% paraformaldehyde as previously described (Garcia-Cabezas et al., 2016; Wang and Barbas, 2018; Trutzer et al., 2019). The brains were then removed from the skull and were cryoprotected in graded

solutions of sucrose and frozen in an isopentane solution (-70°C; Thermo Fisher Scientific). Tissue was sectioned with a freezing microtome in the coronal plane at 40-50 µm, depending on the case, to produce ten matched series. Photographs were obtained (EOS 5D camera, Canon) for experimental library record maintenance. Following slicing and photography, sections were stored at -20°C in antifreeze (30% ethylene glycol, 30% glycerol, and 0.05% sodium azide in 0.1 M PB, pH 7.4).

## **2.6 Immunohistochemical experiments**

### *2.6.1 Brightfield staining*

To identify TRN inhibitory neurons, we used antibodies against the calcium-binding proteins PV and CR which label inhibitory neurons. Previously performed experiments have described these protocols in depth (Zikopoulos and Barbas, 2013; Trutzer et al., 2019). An antibody against SMI-32, which recognized neurofilament proteins, was also used for labelling of excitatory pyramidal projection neurons (Campbell and Morrison, 1989). To summarize, free-floating tissues underwent antigen retrieval with 10mM sodium citrate buffer following washing with 0.01 M PBS. Tissues were incubated in 50mM glycine solution to reduce cross-linking of lipids, 0.3-1% H<sub>2</sub>O<sub>2</sub> solution in the dark for 30 minutes to suppress endogenous peroxidases, and blocking steps, with 0.01M PBS washing steps in between. For PV and CR, blocking was done with 10% normal goat serum, 5% bovine serum albumin, and 0.1% Triton X-100 in 0.01 M PBS for 1 h. For SMI-32, a 2-hour pre-block incubation comprised of 20% BSA, 2% BSA-C, and 9% NGS, and 1% Triton-X was performed. PV and CR tissues were then

incubated for at least a day in either PV or CR mouse monoclonals (1:2000, Swant) followed by at least a 4-hour incubation at 4 °C with biotinylated goat anti-mouse secondary antibodies. For SMI-32, blocking was followed by a three-night incubation in mouse  $\alpha$ -SMI-32 primary antibody (1:10; Sternberger Monoclonals) and a 4-hour incubation in biotinylated goat anti-mouse secondary antibody (Vector; 1:200) in 20% BSA, 2% BSA-C, and 9% NGS, and 0.1% Triton-X. In some cases, an avidin–biotin (AB) peroxidase kit was used to label PV-, CR-, or SMI-32 expressing neurons with 3,3'-diaminobenzidine (DAB). Across all of the antibodies used for immunohistochemistry, control experiments with sections adjacent to those used in experimentation was performed to ensure minimal nonspecific immunoreactivity. Control experiments resulted in no immunohistochemical labeling.

### *2.6.2 Electron microscopy*

EM staining was performed following a double immunohistochemistry staining protocol (Wang and Barbas, 2018). Tissues were selected at the level of MD and LGN for dorsal cases RBN, RBQ, and RBU and ventral cases RBU and RBR. Tissues from RBN, RBQ, and RBU were separated into double-labeling groups containing anti-GABA (gold) and anti-PV (DAB), while tissues from RBR were separated into a double-labeling group containing anti-PV (gold) and anti-CB (DAB). Tissue sections underwent glycine, hydrogen peroxide, and AB incubation to increase the antibody signal, block endogenous peroxidases, and block avid and biotin, respectively. Primary antibody incubation was performed for three days with mouse-anti-PV (PV235, 1:2000 dilution) and rabbit-anti-GABA (ImmunoStar Diasorin 20094, 1:200 dilution) for the anti-GABA (gold) and anti-

PV (DAB) double labeling groups. Meanwhile, mouse anti-CB (Swant CB300, 1:2000 dilution) and rabbit-anti-PV (Swant PV27, 1:2000 dilution) were used for the anti-PV (gold) and anti-CB (DAB) double labeling group. Following this, a secondary antibody incubation was performed for 24 hours with biotinylated goat anti-mouse (Vector BA9200, 1:200 dilution) and gold-conjugated goat anti-rabbit IgG (Aurion Ultra-Small EMS 25811, 1:50 dilution). This staining was performed prior to the introduction of heavy metals to ensure accurate and identifiable labeling of antigens, such as DAB (dark uniform precipitate) and gold particles (black dots). After secondary antibody incubation, the tissues were fixed with 3% glutaraldehyde and 1% paraformaldehyde in 0.1 M PB, washed in 0.05 M glycine (0.1 M PB, 5 min), and incubated in an enhancement conditioning solution (1:10 dilution, 10 min, Aurion). A 90-minute incubation with a silver enhancement kit (R-Gent SE-EM, Aurion) was performed for the intensification of any gold labeling. To further assist in signal amplification and sensitivity, a 60-minute incubation in AB complex (Vector) was completed. Following several 0.1 M PB rinses, AB-HRP and DAB incubation was performed.

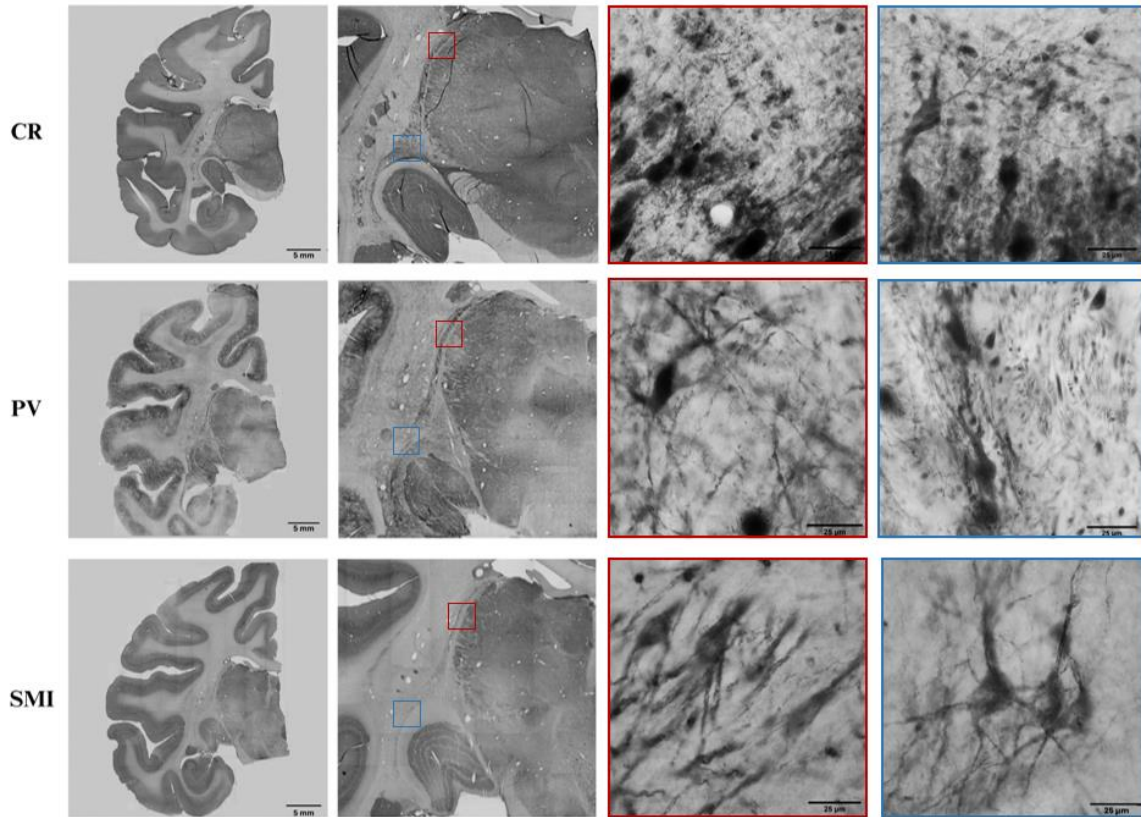
## **2.7 Imaging**

### *2.7.1 Brightfield microscopy*

Utilizing an Olympus BX53 microscope and cellSens Standard imaging software, images from previously stained BF cases were obtained. Overview images portraying entire brain hemispheres were captured with multiple image alignment acquisition at 4x magnification in the coronal plane for each antibody used. As the XY-stage was

navigated, live images were stitched together. Streaks in the image did arise due to lighting adjustment, but staining quality remained intact. Prior to dendritic imaging, a calibration image was obtained by imaging a ruler at 100x magnification to be used in ImageJ analysis. Seven rhesus cases (2 SMI-32, 3 PV, and 2 CR) were selected for BF imaging at 100x magnification. Neurons were selected and imaged only if the antibody staining was preserved to at least the tertiary dendrite. For each suitable cell body and dendritic tree identified, an image series was manually captured with subtle variations in focus to highlight all potential dendritic arborizations. This was repeated for ten to fifteen cell bodies per case in both the d TRN and vTRN. As aforementioned, the criteria for differentiation of dTRN and vTRN is illustrated in Figure 3B. For image analysis, Fiji ImageJ software was used. Prior to insertion of images, the calibration image was inserted with scale adjustment to units of  $\mu\text{m}$ . Image series were then input into ImageJ as an 8-bit stack and Z-projected by the minimum intensity to illustrate all dendritic branching in a single image, allowing for straightforward characterization of cellular architecture and dendritic order.

**Figure 3.** Brightfield Microscopy Image Acquisition



CR, PV, and SMI-32 imaging from brightfield microscopy. Overview images showing the entire hemisphere of the brain which were created by stitching 4x live images together. This view allowed for visualization of the entire TRN, where cells more dorsally (labeled red) and ventrally (labeled blue) could be imaged and analyzed in more detail at 100X magnification.

### *2.7.2 Electron microscopy*

The 3View 2XP System (GATAN) connected to a 1.5 KV scanning electron microscope (GeminiSEM 300, Zeiss) was utilized for block-face imaging. Tissue sections encompassing the thalamus were embedded in resin (Aclar) for preservation purposes. At the site of the monkey TRN, an incision of the tissue 1 mm by 1 mm in size was made and glued onto aluminum pins with conductive epoxy (catalog #CW2400, Chemtronics). An ultramicrotome was then utilized to remove subsequent layers of epoxy and plastic until tissue presence was noted, at which point, silver paint (catalog #16035, Ted Pella) was applied to coat the edges of the tissue. The pin was then loaded into the 3View 2XP system and was automatically sliced in 100 nm sections with an ultramicrotome. As the tissue was sliced, a backscattered detector captured images that were used to place sampling ROIs (20 x 20 to 25 x 25  $\mu\text{m}^2$ ) randomly along the tissue surface. In total, approximately 10 ROI's were selected at each round of imaging, with avoidance of regions dense with myelinated axons or cell bodies. 100 section series for case RBU and RBR were captured for each ROI at pixel size of 2.5 nm, and 200 section series for RBN and RBQ were captured for each ROI at pixel size of 5.0 nm. For each ROI, film negatives were scanned at high resolution (10,000x)(Minolta Dimage Scan Multi II; Konica Minolta, Mahwah, NJ). Image stacks obtained from each ROI were imported into Reconstruct for dendritic and synaptic analyses following alignment and calibration of section thickness. For identification of synaptic structures, classic criteria were utilized (for review, see Peters et al., 1991).

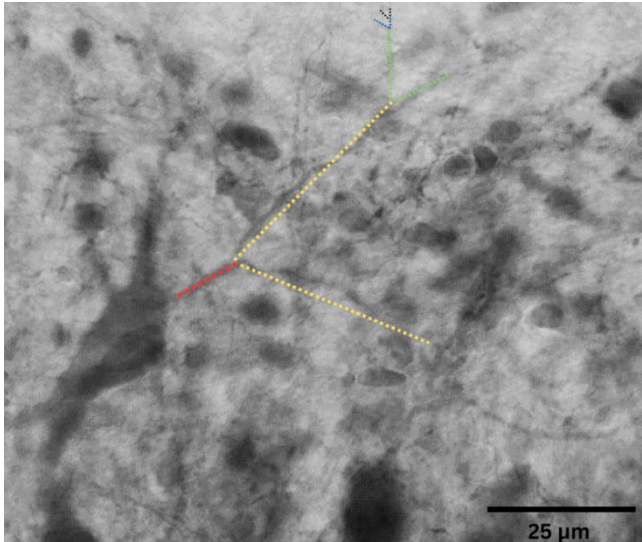
## 2.8 Analysis

### 2.8.1 *Brightfield analysis*

149 neurons were imaged, 74 from dTRN and 75 from vTRN. From these, measurements of thicknesses at each order of dendrite visualizable were obtained and documented. Importantly, thickness measurements on dendritic branches were only made immediately before the next branching event to ensure consistent data acquirement as dendrite tapering was prevalent. For most dendrites, branching thicknesses were recorded up until the quaternary or quinary dendrite, as visualized by the average of maximal dendritic orders captured across cases in Figure 4B. EM data was binned into categories of dendritic order based on the values observed in BF, particularly from SMI-32. Additionally, information pertaining to soma area and diameter was captured to act as a standard of comparison to EM on the basis of dendritic thickness.

**Figure 4.** Sampling and Classification of Dendritic Order

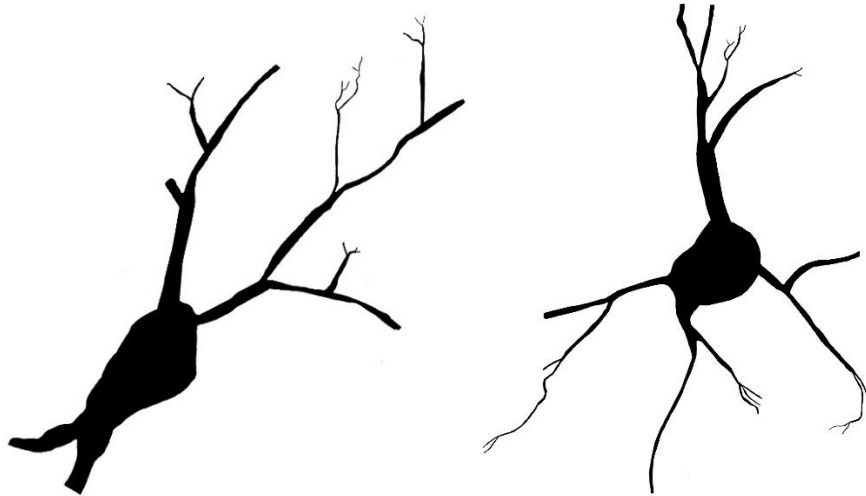
A



B

	<u>Dorsal</u>		<u>Ventral</u>	
	<b>n</b>	<b>Average Order</b>	<b>n</b>	<b>Average Order</b>
<b>SMI-32</b>	30	4.2	32	4.4
<b>PV</b>	23	4.4	21	4.1
<b>CR</b>	21	3.9	22	3.8

C



(A) Image of a typical neuron and dendritic tree viewed at 100X from a ventral view of a CR case. Different orders of dendrites are highlighted as primary, secondary, tertiary, quaternary, and quinary branches are highlighted with red, yellow, green, blue, and black, respectively. (B) Number of different dendritic trees analyzed in SMI-32, PV, and CR. SMI-32 had the most intricate degree of staining as indicated by an average dendritic order analyzed of 4.2 and 4.4 in the dorsal and ventral aspects, respectively. The other two cases had staining that highlighted the dorsal and ventral aspects up to dendritic orders of 4.4 and 4.1 for PV and 3.9 to 3.8 for CR. (C) Drawings of multipolar neurons and their associated dendritic trees from BF.

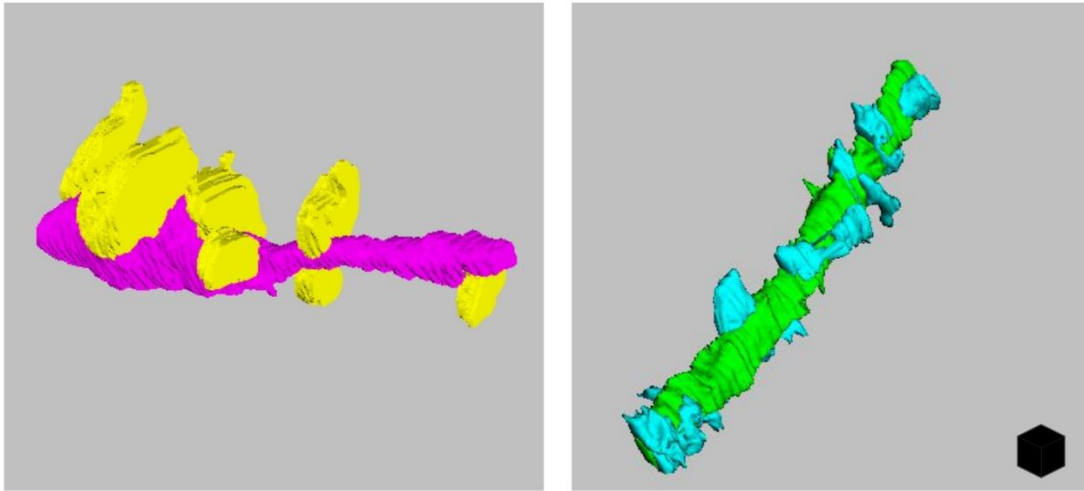
### 2.8.2 *EM analysis*

We viewed TRN dendrites with their associated labeled and unlabeled synapses at high-magnification (10,000x) and photographed them throughout their whole extent (between 100 and 200 serial ultrathin sections). Due to the application of high magnification, dendrites and boutons could be succinctly characterized based on their synaptic features and gold labeling. For analysis, 191 dendrites were followed throughout the ROI image series. 129 dendrites were from the dTRN and 62 from the vTRN, giving an average sampling volume across cases of 2.6% and 12.6%, respectively. Importantly, 95% of dendrites analyzed had GABA or PV labeling, indicating successful immunolabeling of expectedly inhibitory structures throughout the sections. During dendritic analysis, ADTs were calculated and were binned into different dendritic orders based on the BF thicknesses, allowing for analyses to consider proximal and distal orientations. 2,572 boutons synapsing with TRN dendrites were marked and used for calculations of SD (Table 3). Additionally, dendrites and their associated boutons were taken from their 2D serial image EM form and converted into a 3D reconstruction for better visualization of intricate synaptic features. An additional subset of dendrites that portrayed branching behavior were reconstructed for comparison to BF dendritic branching. In total, approximately ten dendrites were fully reconstructed (Figure 5).

**Table 3.** Electron Microscopy Sampling

<b>Case/ ROI</b>	<b>n ROI's</b>	<b>n Dendrites</b>	<b>n Boutons</b>	<b>Length of Dendrites (<math>\mu\text{m}</math>)</b>	<b>Crude Volume (<math>\mu\text{m}^3</math>)</b>	<b>Sampling Volume (%)</b>
<b>RBN</b>	6	17	239	187.0	94.2	2.4%
<b>RBQ</b>	13	90	1277	809.2	202.5	5.0%
<b>RBV</b>	6	22	175	178.7	19.1	0.5%
<b>RBR</b>	5	28	645	273.0	575.7	14.4%
<b>RBU</b>	5	34	236	295.1	431.4	10.8%
<b>dTRN Total</b>	25	129	1691	1174.9	315.8	
<b>vTRN Total</b>	10	62	881	568.1	1007.1	

**Figure 5.** 3D Reconstructions of Synapses in the TRN



Dendrites and their associated synapses were traced throughout EM image series, and 3D reconstructed. The black box in the corner of the reconstruction represents a cube ( $1\mu\text{m} \times 1\mu\text{m} \times 1\mu\text{m}$ ).

### *2.8.3 Bouton analysis*

Of the 2,572 boutons counted at the EM level, 1,094 of these were analyzed from the EM data across all cases in more depth (Table 4). Bouton major and minor diameter, thorn prevalence, mitochondria quantities, vesicle shape, and post-synaptic density (PSD) type were recorded. Aspect ratios, which were related to the shape of boutons, were calculated by taking the ratio between the bouton's minimum and major diameters. Mitochondria were quantified in boutons only directly synapsed on a dendrite of interest. If synapsed through multiple sections, the maximum number of mitochondria seen in a given bouton was recorded. For measurements of PSD, boutons containing gold particles in 3+ sections, even in those not directly synapsed to a dendrite of interest, indicated the presence of GABA or PV depending on the case and provided additional confirmation of

inhibitory synapses and their respective origin. D-, L-, and F-, categorizations discussed in Section 1.4.3 were applied to bouton data obtained.

**Table 4.** Bouton Sampling

Case/ Region	Total Dendrites	Total Length of Dendrites ( $\mu\text{m}$ )	Total Boutons
<u>RBN</u>	14	145.4	185
<u>RBQ</u>	13	145.4	237
<u>RBV</u>	16	139.5	148
<u>RBR</u>	13	146.2	137
<u>RBV</u>	15	150.9	387
Dorsal Total	33	430.3	570
Ventral Total	28	297.1	524

## 2.9 Statistics

Data was evaluated in Excel, JMP, or Python, depending on the analysis performed. For determining the difference between dorsal and ventral data distributions, Kolmogorov–Smirnov (K-S) tests were used. ANOVA and post-hoc Tukey tests were done to test for differences among different orders of dendrites. Furthermore, for clustering of dendrites and boutons into populations based on features such as size and shape, k-means cluster analysis was performed. Across all statistical analyses p-values < 0.05 were taken as statistically significant.

### **3. RESULTS**

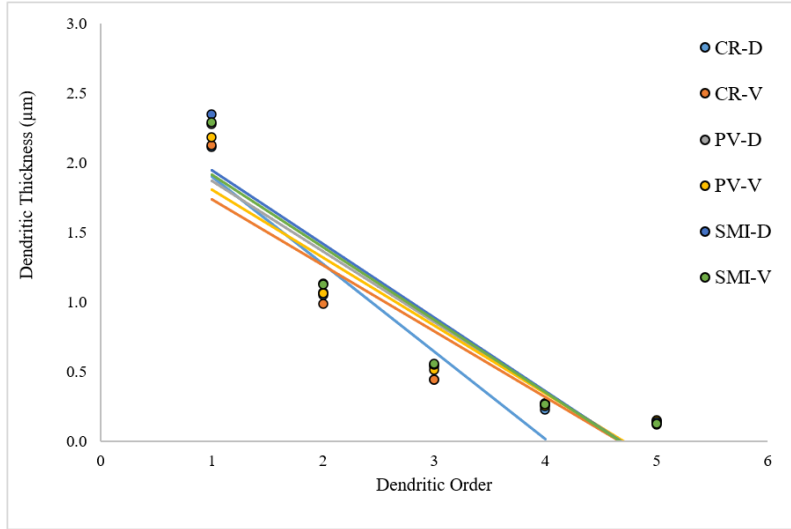
#### **3.1 Dendritic branching and categorization of dendritic order**

Using BF microscopy, thicknesses were measured at each order of dendrite prior to subsequent branching points in the dTRN and vTRN. For each antibody, the dorsal and ventral thicknesses were averaged separately to observe clustering by dendritic order (Figure 6A). This demonstrated a distinct downward trend as dendrites that were located more distally were thinner than those located more proximally. Particularly, the transition from one branch to the next resulted in a reduction in thickness by approximately half. The average values for primary, secondary, tertiary, quaternary, and quinary were 2.224, 1.071, 0.505, 0.256, and 0.134  $\mu\text{m}$  across all antibodies used. Of note, there was no statistically significant difference between ventral and dorsal branch thicknesses.

Dendrites from the EM gave a continuous range of ADTs, covering a wide array of sizes (0.14  $\mu\text{m}$ , < thickness < 2.72  $\mu\text{m}$ ), with dorsal and ventral averages of 0.543 and 1.33  $\mu\text{m}$ , respectively (Figure 7A). Differences in ADTs of dorsal and ventral dendrites was confirmed when observing the statistically significant difference shown in Figure 7B. This significance between the dTRN and vTRN thickness EM measurements deviates from what was seen in the BF likely due to a lack of context about where the dendrite may exist along the dendritic tree.

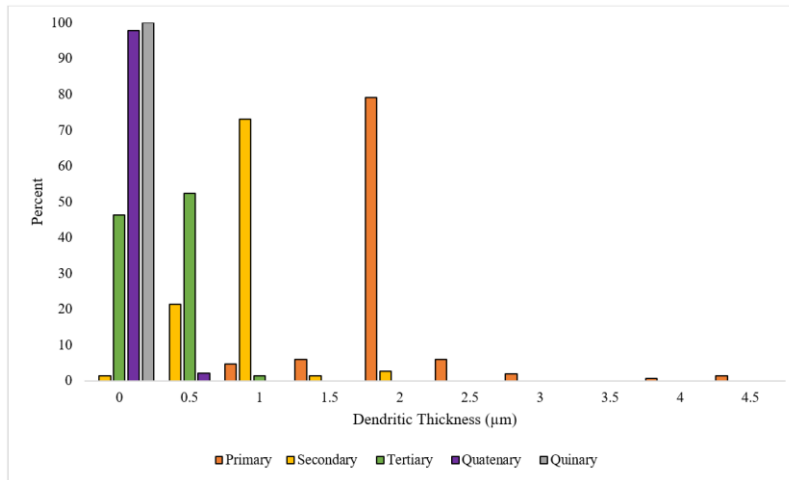
**Figure 6.** Thickness of Dendrites Across Dendritic Order

A



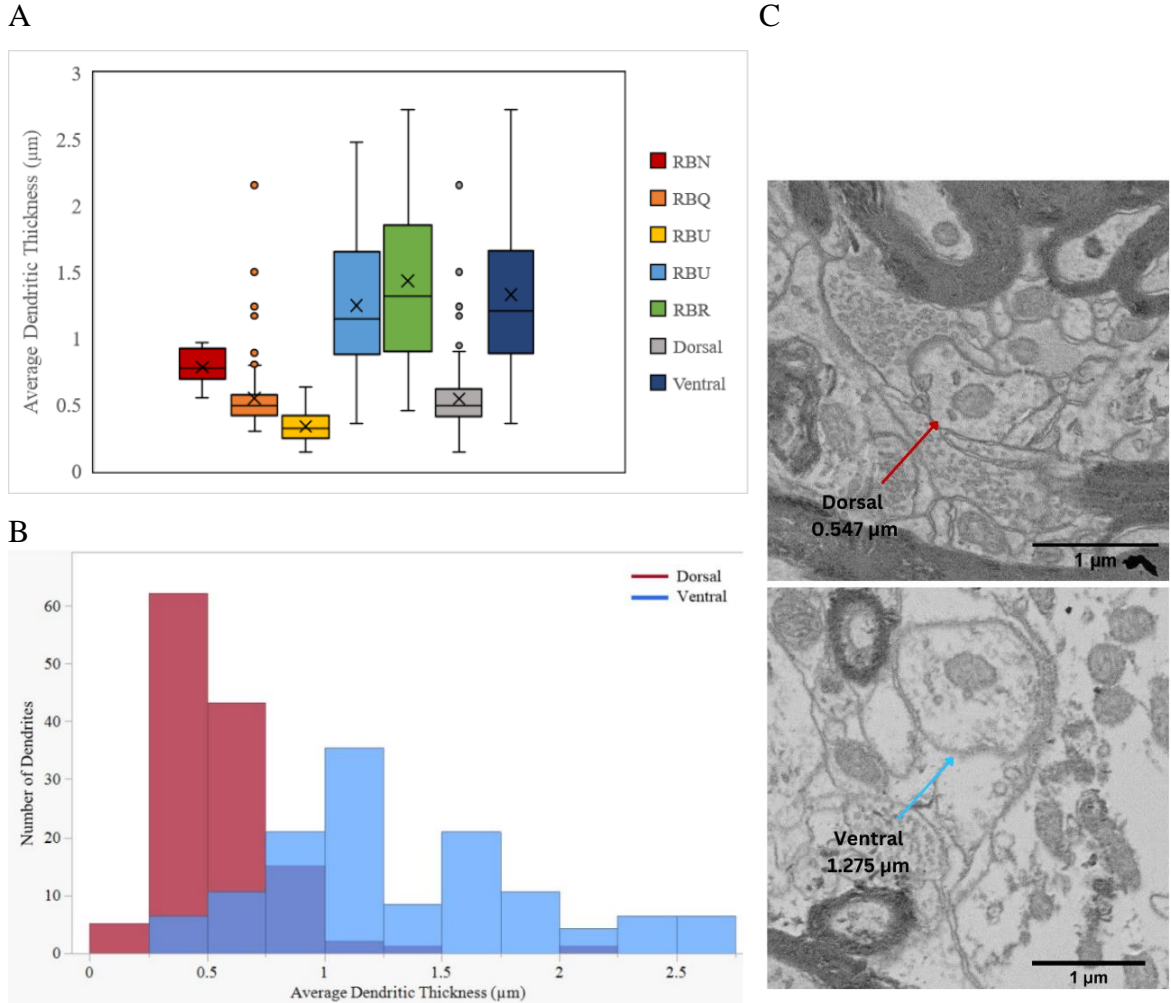
Case ID	R <sup>2</sup>	r
CR-D	0.916	-0.957
CR-V	0.839	-0.916
PV-D	0.851	-0.922
PV-V	0.856	-0.925
SMI-D	0.858	-0.926
SMI-V	0.816	-0.903

B



(A) Average thicknesses of CR, PV, and SMI-32 dendrites across order. The primary, secondary, tertiary, quaternary, and quinary orders were averaged for each antibody used: dorsal CR (2.116, 1.048, 0.439, 0.224, and N/A µm), ventral CR (2.127, 0.988, 0.440, 0.273, and 0.120 µm), dorsal PV (2.275, 1.070, 0.536, 0.259, and 0.144 µm), ventral PV (2.183, 1.063, 0.512, 0.252, and 0.147 µm), dorsal SMI-32 (2.350, 1.132, 0.546, 0.267, and 0.135 µm), and ventral SMI-32 (2.293, 1.127, 0.557, 0.260, and 0.125 µm). CR dorsal, CR ventral, PV dorsal, PV ventral, SMI-32 dorsal, and SMI-32 ventral had r values of 0.957, 0.916, 0.922, 0.925, 0.926, and 0.903, respectively, indicating a strong negative correlation between dendritic thickness and order. p-values of 0.999, 0.938, and 0.512 for CR, PV, and SMI-32 indicated no difference between dTRN and vTRN. (B) Bar chart demonstrating the percentages of primary, secondary, tertiary, quaternary, and quinary dendrites that correspond to various thicknesses across all BF cases.

**Figure 7.** Average Dendritic Thickness in the dTRN and vTRN

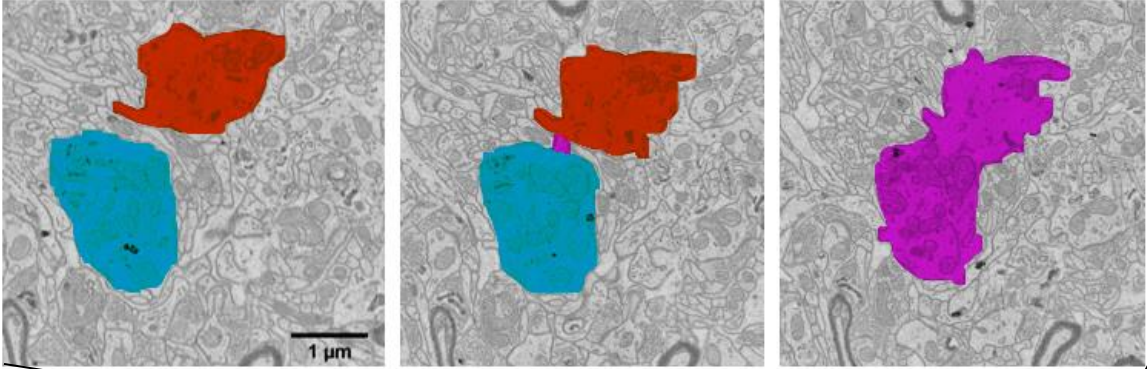


(A) Box-and-whisker plot displaying the ADTs across cases from EM data. The average value is denoted by an “x.” From RBN (red), RBQ (orange), RBU dorsal (yellow), RBU ventral (blue), and RBR (green), the averages were 0.782, 0.549, 0.336, 1.245, and 1.433  $\mu\text{m}$ , respectively. Averaging the dorsal cases and the ventral cases separately gave values of 0.543 and 1.33  $\mu\text{m}$ , respectively. Importantly, ADTs ranged from (0.14  $\mu\text{m}$ , < thickness < 2.72  $\mu\text{m}$ ,) across all cases, (0.14  $\mu\text{m}$ , < thickness < 2.15  $\mu\text{m}$ ,) in dTRN and (0.36  $\mu\text{m}$ , < thickness < 2.72  $\mu\text{m}$ ,) in vTRN. (B) Histogram demonstrating the difference in dorsal and ventral ADTs. Utilizing a K-S test, a statistically significant relationship, as determined by a p-value of <0.0001 was found between the dTRN and vTRN ADTs. (C) EM images illustrating appearance of dTRN and vTRN dendrites with ADT’s close to averages noted. Dendrites with their corresponding thickness at the section shown are labeled in red (dorsal) and blue (ventral).

BF provided a zoomed-out view of the cell and its' associated dendritic tree, sometimes even up to the fifth branching point. Since the EM images are small randomly sampled regions along the dendritic tree, it is plausible in a large sample size that dendritic branching would be encountered at the EM level. We sampled nine dendrites in total, three from the vTRN and six from the dTRN, giving a total sampling length of 125  $\mu\text{m}$ . From all dendrites we sampled across the TRN, 7.17% of the sampling length was from these branching dendrites. For all the data, the branching segments did have reduced thickness when compared to the main branches. The dendrites did not necessarily branch by half in all dendrites analyzed, but most did reduce close to half, barring a few exceptions (Figure 8B). Any difference noted between BF and EM branching could be explained by the higher resolution of EM images, which allowed for more accurate measuring. At this level, we didn't observe any trends with SD between the branched and combined segments likely due, once again, to lack of context pertaining to dendritic order.

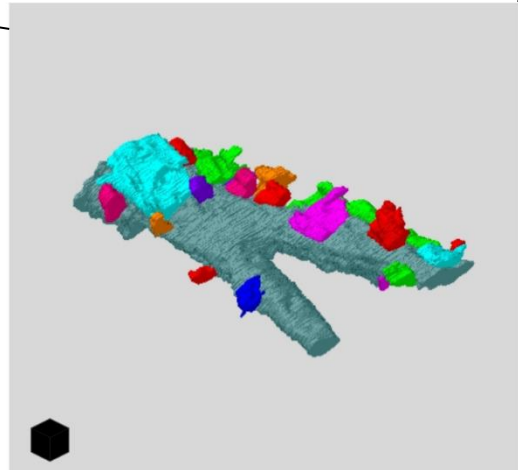
**Figure 8.** 3D Reconstruction of Dendritic Branching from Electron Microscopy

A



B

Combined Branch	First Branch	Second Branch
0.553	0.362	0.295
1.500	0.798	0.788
0.889	0.567	0.399
2.155	1.238	1.169
0.660	0.640	0.345
0.787	0.443	-
1.572	1.166	0.457
1.722	0.994	0.827
1.208	1.136	0.580

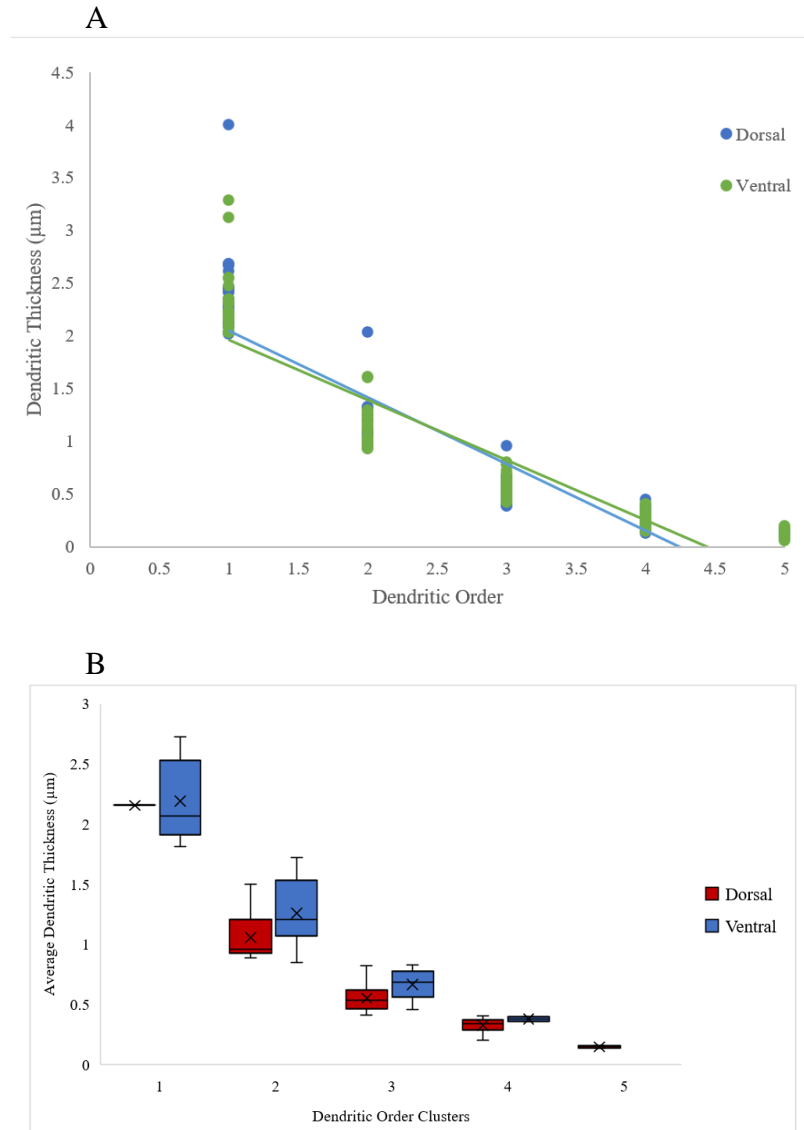


(A) A series of images (top) showing the joining of two separate dendrites (red and blue) into one combined branch (purple), indicative of dendritic branching behaviors. When the dendrites and boutons associated with this branch were traced throughout the entirety of the ROI, a 3D reconstruction was made (bottom right). The dendritic branches are shown in grey while the synapses are shown in multiple colors. The black box in the corner of the reconstruction represents a cube ( $1\mu\text{m} \times 1\mu\text{m} \times 1\mu\text{m}$ ). (B) Table demonstrating how thickness changes as dendritic branching occurred. “-“ denotes an unknown thickness due to dendritic branching that occurred partially out of view of the screen.

Despite only having a small sample of EM dendrites that portray branching behaviors, thicknesses determined for different dendritic orders in BF can be applied to the remaining EM data that did not show direct branching. Serving a multifaceted purpose, this would help us to gain context of dendritic order within dendritic tree, observe differences bouton quantity and type in proximal and distal dendrites, and identify if thicknesses in the dTRN and vTRN truly differ. For this analysis, only SMI-32 staining was used because it highlighted the structure of the dendritic tree in detail as it showed more intricate staining distally compared to PV and CR (Figure 4). In Figure 6, it was determined that there was a lack of statistical significance between SMI-32 dorsal and ventral thicknesses across dendritic order. As such, the dorsal and ventral SMI-32 values for primary, secondary, tertiary, quaternary, and quinary were averaged into 2.322, 1.129, 0.552, 0.264, and 0.130  $\mu\text{m}$ , respectively (Figure 9A). Based on these averages, the ADTs calculated at the EM level were binned into five categories. To confirm the EM groupings identified, a k-means cluster analysis was performed on SMI-32 data; however, it suggested different centers than that of the raw data. Particularly, it indicated that the centers for primary, secondary, tertiary, quaternary, and quinary should be 3.073, 2.24, 1.11, 0.534, and 0.22  $\mu\text{m}$ , respectively. While these numbers do not match the raw data, it provides useful information. Examining the thickness of the primary dendrite, it is clear that the true average, 2.32  $\mu\text{m}$ , compared to that of the k-means averages, 3.073  $\mu\text{m}$ , are different. While we consistently took measurements of primary thickness immediately prior to branching into secondary, it is an innate feature of dendrites to taper rapidly as they move away from the soma as this maximizes current transfer (Bird and

Cuntz, 2016). Tapering was especially pronounced as the cell body tapered down to the primary dendrite. This resulted in more variation in thicknesses among primary dendrites, explaining the difference between the true data and k-means. Interestingly, both the original data and the k-means clusters showed that dendritic thickness were reduced by approximately half when moving from one branch to the next. However, the exact values did not match, indicating that the dendritic thicknesses values may be more continuous than clustered, which has been previously shown in other thalamic nuclei (Kultas-Ilinsky et al., 1997). In total, 14 EM dendrites were primary, 46 were secondary, 98 were tertiary, 31 were quaternary, and 2 were quinary. The ventral cases comprised most of the primary and secondary dendrites with percentages of 92.86% and 80.43%, respectively. The dorsal dendrites made up the majority of tertiary, quaternary, and quinary dendrites with percentages of 89.80%, 93.55%, and 100%, respectively (Figure 9B). This solidifies the notion that the differences in thickness between the dTRN and vTRN from the EM were likely not due to profound biological differences but rather due to differences in dendritic order.

**Figure 9.** Dendritic Order Clustering of Electron Microscopy



(A) Thicknesses from SMI-32 dorsal and ventral BF measurements. dTRN and vTRN showed  $r$  values of 0.911 and 0.918, respectively. Lack of statistical significance in dorsal and ventral was determined by a  $p$ -value of 0.512. As a result, the dorsal and ventral SMI-32 values for primary, secondary, tertiary, quaternary, and quinary were averaged giving values of 2.322, 1.129, 0.552, 0.264, and 0.132  $\mu\text{m}$ , respectively. (B) EM data categorized into dendritic order by thickness based on SMI-32 BF results. The ventral cases comprised most of the primary and secondary dendrites while dorsal dendrites made up the majority of tertiary, quaternary, and quinary dendrites.

### 3.2 Soma analysis

In order to utilize the SMI-32 BF data as criteria for categorizing EM thicknesses into different dendritic orders, we needed to ensure there was a standard for comparing these techniques. To do this, we made use of somata. These are easily identifiable in both BF and EM, and if soma areas and diameters are similar, it confirms EM clustering approach. Avoiding any duplicate cell body measurements, average cell body area in dTRN and vTRN were determined to be  $233.99 \pm 43.0 \mu\text{m}^2$  and  $343.05 \pm 96.4 \mu\text{m}^2$  for SMI-32,  $255.72 \pm 65.2 \mu\text{m}^2$  and  $285.26 \pm 70.9 \mu\text{m}^2$  for PV, and  $172.34 \pm 57.9 \mu\text{m}^2$  and  $185.19 \pm 57.7 \mu\text{m}^2$  for CR. SMI-32 demonstrated a statistically significant relationship between the somata of the dTRN and vTRN ( $p < 0.0001$ ); however, this was not the case in CR ( $p = 0.9453$ ) or PV ( $p = 0.6907$ ) staining. The SMI-32 significance may be a result of small sampling at this level as the dendritic thicknesses across order were shown to have no difference in the dTRN or vTRN. For the most part though, these values matched what was seen at the EM level, providing confirmation for the application of BF data to EM clustering. However, it does appear that dTRN cells are slightly smaller than that of vTRN overall, but additional sampling should be done to confirm this. Furthermore, most of the cells identified at the BF level were bipolar or multipolar with either round or fusiform somata, which are phenotypes previously described (Cox et al., 1996; Lee et al., 2007).

### 3.3 Synaptic density

To characterize the synaptic features at the EM level, we first calculated the SD for each of the dendrites analyzed (Figure 10A). SD measurements gave a continuous

range of values, covering a wide array of sizes from 0.22 boutons/ $\mu\text{m}$  to 5.889 boutons/ $\mu\text{m}$ , with dorsal and ventral averages of 1.460 and 1.564 boutons/ $\mu\text{m}$ , which was determined to be a statistically significant difference as shown in Figure 10B.

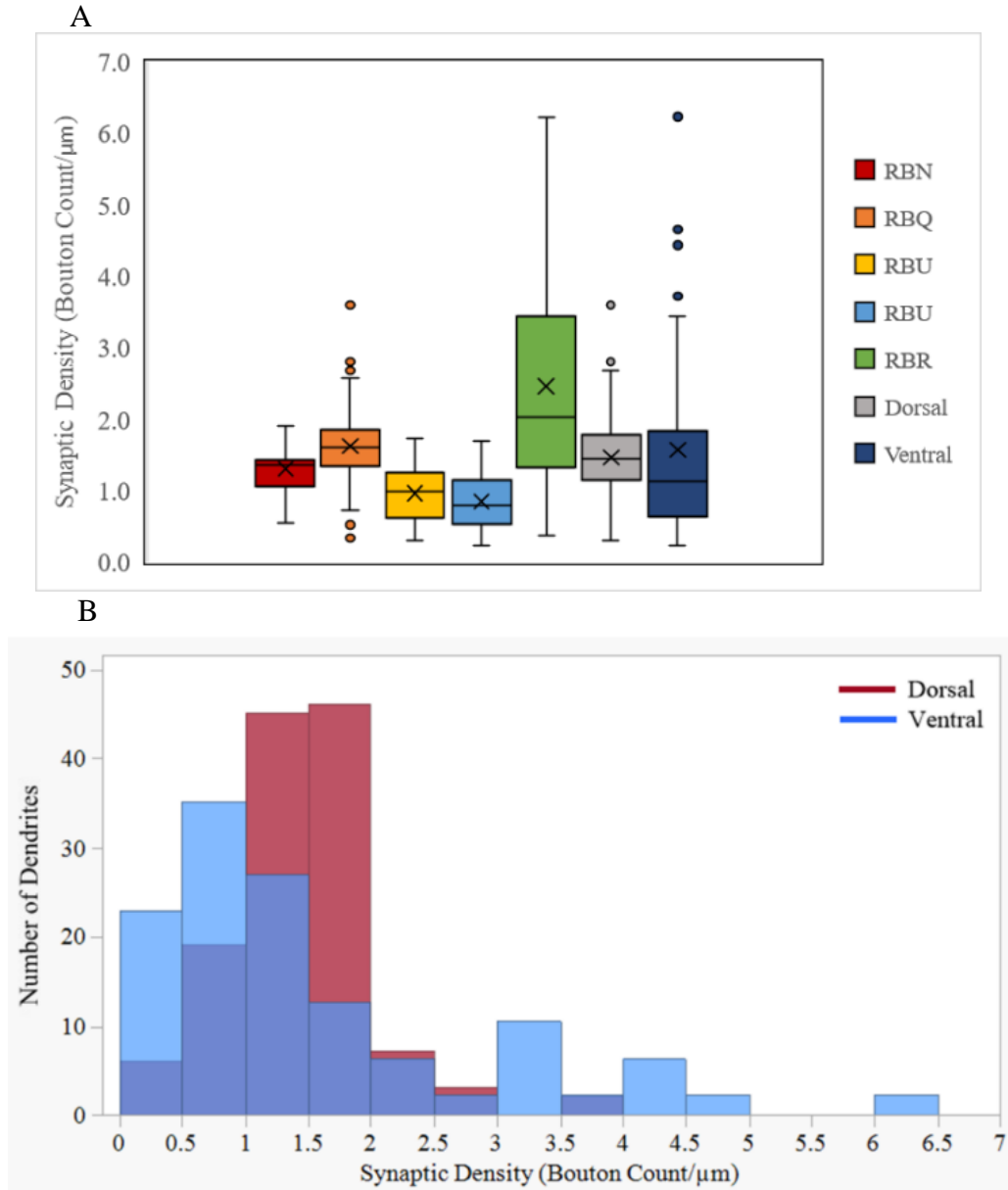
There have been trends in literature noting relationships between bouton size and dendritic order (Liu and Jones, 1999; Zikopoulos and Barbas, 2006). Therefore, we wanted to see if there were also trends between SD and dendritic order. To determine this, values of major bouton diameters and SD were shown for both the dorsal and ventral data (Figure 11A). These variables appear to be weakly correlated in the dTRN but more moderately correlated in the vTRN. Potentially, this be due to innate differences between the dTRN and vTRN; however, given that most of the ventral dendrites are proximal and larger while the dorsal are distal and smaller, there may be interference (Liu and Jones, 1999). To distinguish this, we compared the dTRN and vTRN's SDs at a given order of dendrite (Figure 11B). This approach controlled for dendritic order, allowing for a true comparison of dTRN and vTRN to be made.

On average, primary, secondary, tertiary, quaternary, and quinary dendrites had SDs of 2.31, 1.48, 1.51, 1.17, and 0.47 boutons/ $\mu\text{m}$ , respectively. From visualizing the results in Figure 11B, it appears that on more distal branches, SD drops for the vTRN but not for the dTRN. For the primary, secondary, tertiary, and quaternary dendrites, the average SD of vTRN was 2.35, 1.52, 0.94, and 0.48 boutons/ $\mu\text{m}$ . Meanwhile, for secondary, tertiary, quaternary, and quinary orders, the average SD of dTRN was 1.31, 1.57, 1.22, 0.47 boutons/ $\mu\text{m}$ . In order to determine if there is a statistically significant decrease in SD as more distal branches are encountered, we calculated the differences in

SD between orders of dendrite for vTRN separately from dTRN. Importantly, in our analysis of vTRN, we only had a large enough population from primary, secondary and tertiary dendrites, and from dTRN, we only had a large enough population from secondary, tertiary, and quaternary to run the analysis. Doing an ANOVA on vTRN SDs between orders of dendrite determined that the decrease from the primary to the tertiary dendrite showed a statistically significant reduction in SD. However, in the dTRN, no statistically significant relationship was determined between groups of dendritic order on the basis of their SDs.

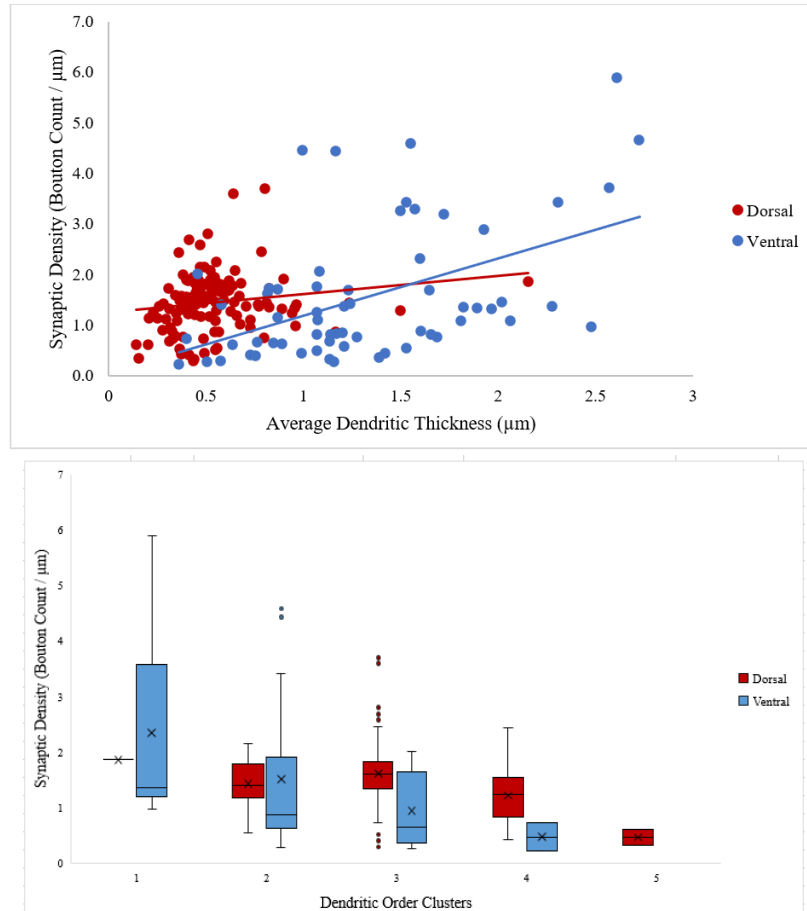
When comparing the dTRN and vTRN at different dendritic orders, the tertiary order showed a statistically significant difference between dTRN and vTRN ( $p=0.013$ ), with the dTRN being higher. This also seems to be the case for other orders of dendrites, but in a nonsignificant way. Conflictingly, in Figure 10B, ventral SDs were identified as being significantly higher than that of the dorsal SD. This is likely due to the higher SDs located on primary dendrites which were sampled almost entirely from the ventral aspect.

**Figure 10.** Synaptic Density in the dTRN and vTRN



(A) Box-and-whisker plot displaying the SD across cases from EM data. The average value was denoted by an "x." From RBN (red), RBQ (orange), RBU dorsal (yellow), RBU ventral (blue), and RBR (green), the averages were 1.300, 1.615, 0.955, 0.841, and 2.442 boutons/ $\mu\text{m}$ , respectively. The dorsal and ventral cases had means of 1.460 and 1.560 boutons/ $\mu\text{m}$ , respectively. (B) Histogram demonstrating the difference in dorsal and ventral SD. Utilizing a K-S test, a statistically significant relationship was found between the dorsal and ventral dendritic thicknesses as confirmed by a p-value of 0.0021.

**Figure 11. Dendritic Thickness and Synaptic Density**



(A) Correlation between dendritic thickness and SD. dTRN demonstrates a weak relationship between ADT and SD while vTRN demonstrates a moderately strong relationship based on correlation coefficients of  $r = 0.158$  for dorsal and  $r = 0.492$ . (B) SD variations across changes in dendritic order. The average value was denoted by an “x.” In the dTRN secondary, tertiary, quaternary, and quinary correspond to average SDs of 1.31, 1.57, 1.22, 0.47 boutons/ $\mu\text{m}$  and in the vTRN primary, secondary, tertiary, and quaternary average SDs were 2.35, 1.52, 0.94, and 0.48 boutons/ $\mu\text{m}$ . A one-way ANOVA with a post-hoc Tukey test showed lack of statistical significance was seen between dTRN secondary and tertiary order (0.299), tertiary and quaternary order (0.117), and secondary and quaternary order (0.868). Meanwhile, for vTRN, lack of statistical significance was seen between primary and secondary order (0.185) and secondary and tertiary order (0.440), but not between primary and tertiary orders (0.010). K-S test determined differences in dorsal and ventral SDs within a given order of dendrite. Comparing dTRN and vTRN in secondary, tertiary, and quaternary gave p-values of  $p=0.065$ ,  $p=0.013$ , and  $p=0.1541$ , respectively.

### **3.4 Characterizing the bouton: Size, shape, mitochondria, and origin**

#### *3.4.1 Size*

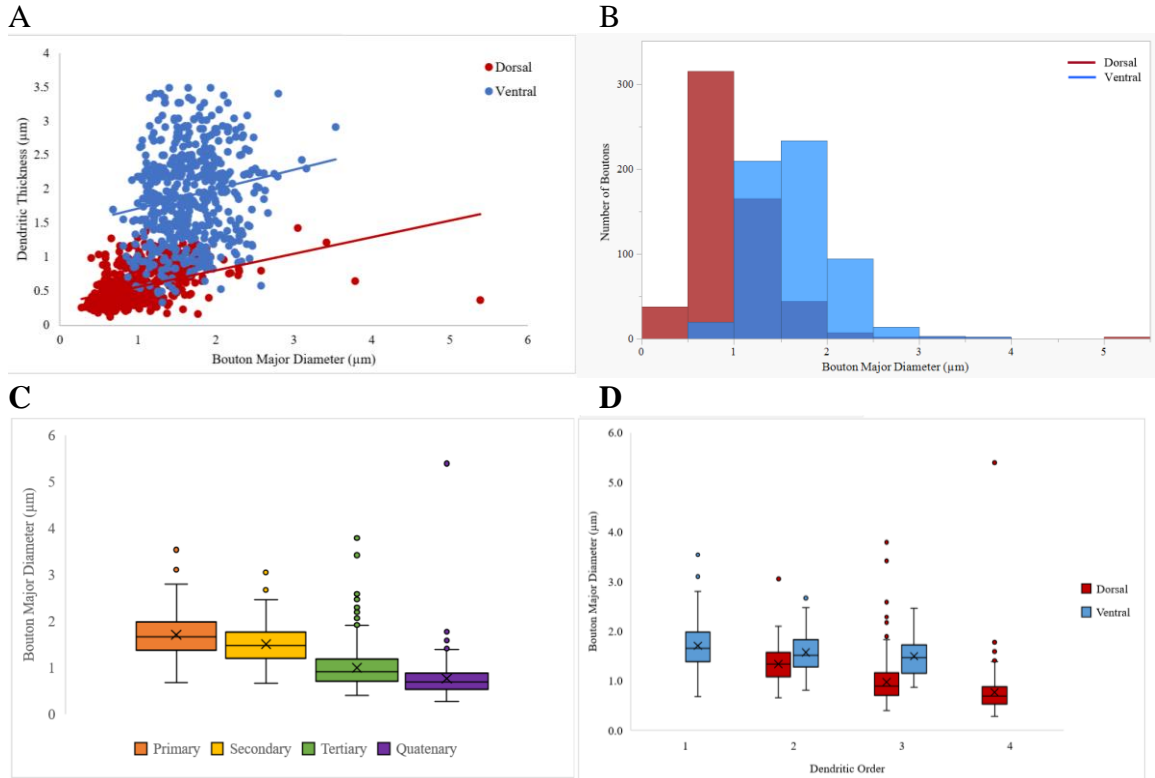
61 dendrites and their associated 1,094 boutons from the EM were examined for this analysis. Of these, clustering showed that there was 11 primary, 20 secondary, 26 tertiary, and 14 quaternary dendrites that each had 319, 258, 370, and 147 boutons, respectively. No quinary dendrites were represented in the bouton analysis. In literature, it has been suggested that larger boutons synapse with larger more proximal dendrites and smaller boutons synapse with smaller distal dendrites; however, in the prefrontal pathway, small and large boutons synapse similarly on both proximal and distal dendrites (Liu and Jones, 1999; Zikopoulos and Barbas, 2006). In order to identify which trend our data exhibited and if this differed in the dTRN and vTRN, we compared bouton major diameter and dendritic size (Figure 12A). From this, a moderate trend was identified for the dTRN while the vTRN illustrated a weak relationship. The boutons sizes from the dTRN and vTRN were then compared (Figure 12B), showing a statistically significant relationship between the distributions ( $p < 0.0001$ ).

Dendritic sizes were then converted into categories of dendritic order that allowed for the bouton major diameters to be organized more proximally and distally (Figure 12C). The mean bouton diameter for primary, secondary, tertiary, and quaternary was 1.71, 1.51, 1.00, and 0.77  $\mu\text{m}$ . Bouton diameters were shown to be statistically significant across dendritic orders ( $p < 0.0001$ ), indicating that overall, bouton diameter gets smaller more distally. We then examined how vTRN differs by its' bouton diameter across each dendritic order separate from the dTRN (Figure 12D). In the vTRN, a statistically

significant difference was identified between the primary and secondary order, but not between the tertiary and the primary/secondary. In the dTRN, the difference between secondary, tertiary, and quaternary orders were all statistically significant ( $p < 0.0001$ ). This suggests that vTRN and dTRN differ on how bouton diameter changes as more distal branches were approached. The vTRN shows little changes in bouton major diameter with changes in dendritic order, except for between the primary and secondary order. The means for primary, secondary, and tertiary which are 1.71, 1.57 and 1.49  $\mu\text{m}$  confirm this further. Meanwhile in the dTRN, we saw decreases in bouton diameter as more distal branches were approached. The means for secondary, tertiary, and quaternary which are 1.34, 0.97, and 0.77  $\mu\text{m}$  confirm this further. To confirm if the dTRN and vTRN bouton diameters differed at a given dendritic order, secondary and tertiary dendrites, which had a mixed population of both dTRN and vTRN, were examined. From this, the dTRN and vTRN was determined to have significantly different bouton diameters when examining secondary and tertiary branches.

Bouton populations were continuous on the basis of size, covering a wide range ( $0.124 \mu\text{m} < \text{diameter} < 5.392 \mu\text{m}$ ). Through a k-means cluster, two distinct bouton sizes were shown to exist. These corresponded to small boutons (mean diameter ( $\mu\text{m}$ )  $\pm$  SD,  $0.912 \pm 0.27$ ) and larger boutons (mean diameter ( $\mu\text{m}$ )  $\pm$  SD,  $1.820 \pm 0.40$ ). Based on this criterion, 58.0% of boutons sampled across the TRN were small and 42% were large. In the dTRN, 85.4% were small and 14.6% were large while in the vTRN, only 28.4% were small while 71.6% were large, which is a difference reflected in Figure 12B.

**Figure 12.** Characterization of Bouton Size



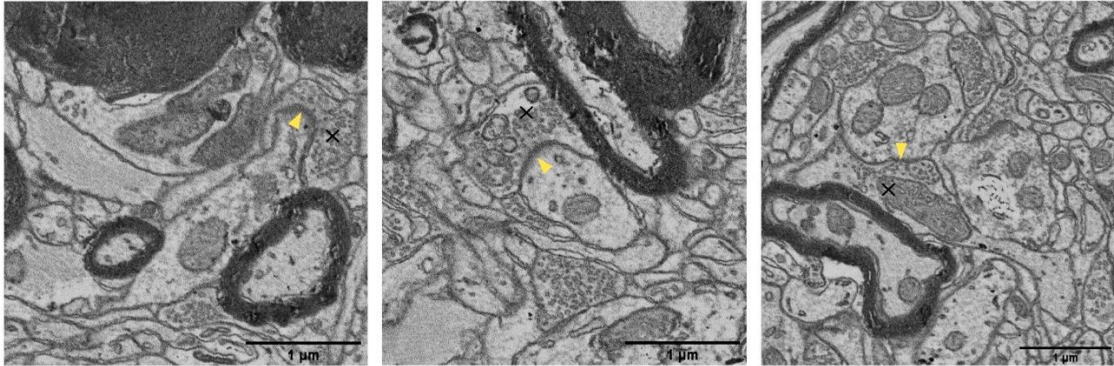
(A) Relationship between bouton major diameter and dendritic thickness. Correlation coefficients were calculated as 0.426 for dTRN and 0.1163 for vTRN. (B) Histogram demonstrating the difference in dorsal and ventral bouton sizes. A K-S test showed statistically significance between the dorsal and ventral dendritic thicknesses ( $p$ -value  $<0.0001$ ). (C) Box-and-whisker plot demonstrating how bouton diameter changes across dendritic order. The average value was denoted by an “x.” Mean bouton diameter for primary, secondary, tertiary, and quaternary was 1.71, 1.51, 1.00, and 0.77  $\mu\text{m}$ . Bouton diameters were shown to be statistically significant across dendritic order as determined by ANOVA ( $P < 0.0001$ ). Post hoc Tukey test confirmed this between all orders. (D) Box-and-whisker plot demonstrating how bouton diameter changes across dendritic order separated by dTRN and vTRN. The average value was denoted by an “x.” Mean bouton diameter for primary, secondary, and tertiary in the vTRN were 1.71, 1.57 and 1.49  $\mu\text{m}$  while the secondary, tertiary, and quaternary in the dTRN were 1.34, 0.97, and 0.77  $\mu\text{m}$ . In the dTRN, ANOVA and post-hoc Tukey revealed statistical significance for the bouton diameters between all orders of dendrites ( $p < 0.0001$ ). vTRN showed significant relationship between primary and secondary order ( $p = 0.0014$ ) but not between primary and tertiary ( $p = 0.0798$ ) or secondary and tertiary orders ( $p = 0.7200$ ). A K-S test between the dorsal and ventral bouton diameters in the secondary and tertiary orders gave  $p$ -values of  $p = 0.0008$  and  $p < 0.0001$ , respectively.

### *3.4.2 Shape*

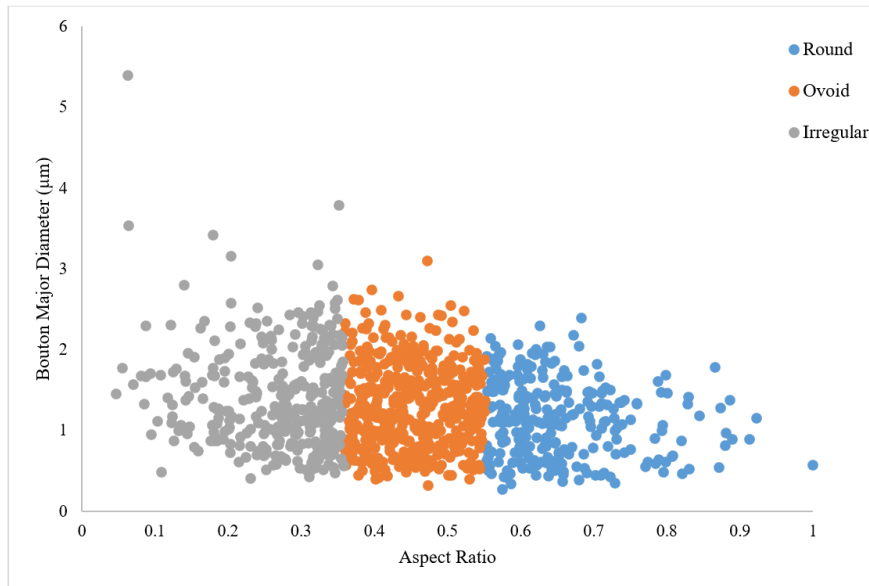
Aspect ratios, which provide information about shape, were calculated using the bouton minor and major diameter. Based on previous findings, small boutons tend to have rounder shapes while larger boutons have a greater variety of shape, being round, ovoid, or irregular (Zikopoulos and Barbas, 2006). Aspect ratios range anywhere from zero to one, where zero suggests irregularity and one signifies roundness. Based on a k-means cluster analysis, categories into irregular, ovoid, and round shapes were determined based on aspect ratios. From this, 31% of sampled boutons were irregular, 43.7% were ovoid, and 25.3% were round. Relative to size, 66.4% of the round, 56.3% of ovoid, and 54.7% of the irregular boutons are also considered to be small while the remaining were large, which is reflected in Figure 13B.

**Figure 13.** Characterizing Bouton Shape and Size

A



B



(A) EM images of boutons marked with black X to show round (left), ovoid (middle), or irregular bouton shapes (right). Respective aspect ratios are 0.814, 0.495, and 0.180. Yellow arrow denotes the location of synapsing. (B) Scatterplot displaying the relationship between bouton shape and size. Irregular (grey), ovoid (orange), and round boutons (blue) showed clustering on the basis of their aspect ratios.

### 3.4.3 Mitochondria and origin

Based on the D-, L-, and F- terminal categorizations for boutons, PSD and mitochondrial content helped to derive information about the origin of boutons. A common notion amongst studies that examine bouton characteristics is that larger boutons tend to have a greater mitochondrial content and tend to synapse more proximally to the cell body (Liu and Jones, 1999; Zikopoulos and Barbas, 2007a). We already have discussed how larger boutons were seen more proximally (Figure 12C and 12D). Therefore, we also wanted to confirm whether large size is related to increased mitochondrial content. Of the large boutons examined at the TRN, 46.2% boutons had 2+ mitochondria while the remaining 53.8% had boutons with 0-1 mitochondria. Of the small boutons examined at the TRN, only 10.0% had 2+ mitochondria while the remaining 90% had boutons with 0-1 mitochondria. Therefore, this differentiation of mitochondria between small and large dendrites appears to match the known trend ( $p < 0.0001$ ).

Across the TRN, 97.9% of boutons were excitatory, 97.4% in dorsal and 98.3% in ventral. This further subdivided into 73.7% of boutons were asymmetric with 0-1 mitochondria (D-terminal type), 24.2% were asymmetric with 2+ mitochondria (L-terminal type), and 2.2% were symmetric synapses (F-terminal type). In the dorsal aspect, 89.3% were D-terminal, 8.1% were L-terminal, and 2.6% were F-terminal. In the vTRN, 56.7% of boutons were D-terminal, 41.6% were L-terminal, and 1.7% were F-terminal (Figure 13A). Since boutons arising from the D-terminal group are smaller and make up

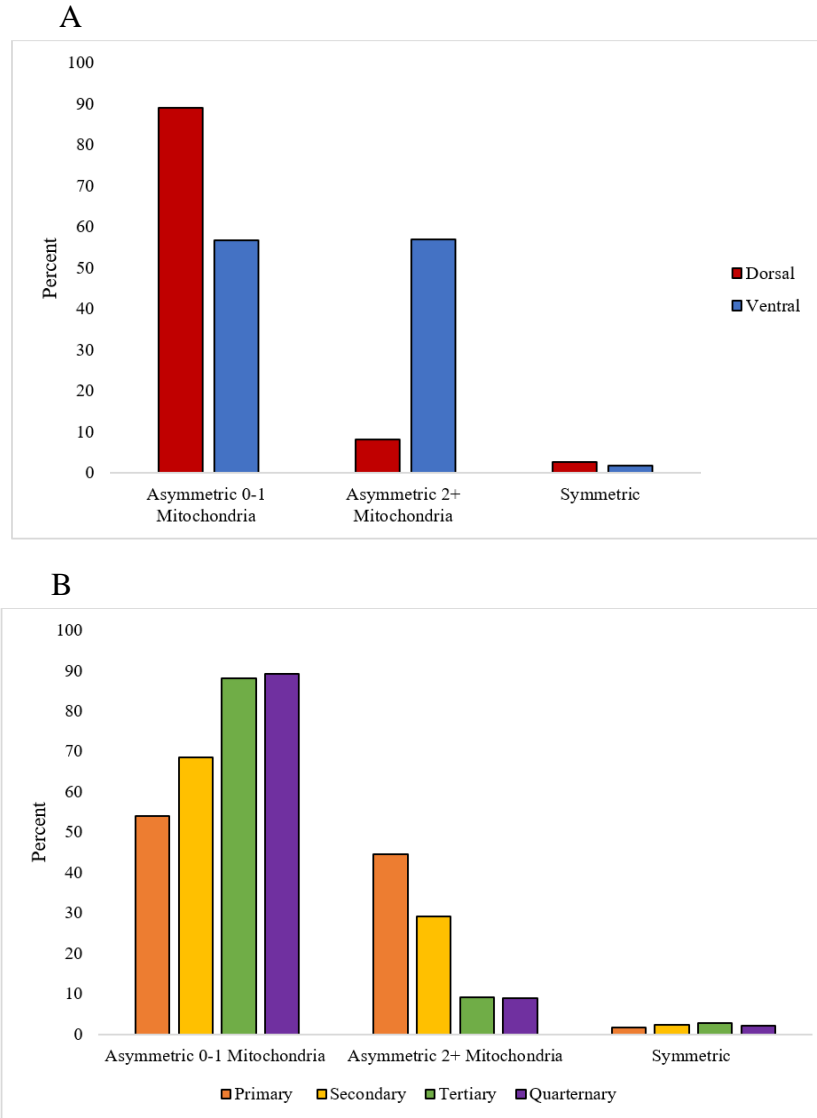
most of the boutons sampled dorsally, this indicates that dorsal boutons are smaller than ventral boutons, a trend which was previously confirmed in Figure 12D. Boutons from the amygdala and SC fell into the asymmetric with 2+ mitochondria group and were counted if they were large in size and had at minimum five mitochondria. In some cases, boutons with four mitochondria but sizes within the largest 10% of sizes (greater than 2.00  $\mu\text{m}$ ) were counted. Out of all of the boutons sampled, the amygdala and SC boutons only made up 2.5%. Within the L-terminal group, 10.2% of boutons were from the amygdala or SC across the entire TRN, with 8.7% from dTRN and 10.6% from vTRN. The difference in dTRN and vTRN proportions may be due to more widespread projections from the SC to the vTRN as needed for the modulation of the transmission of visual signals to the cortex. Boutons from the BG group fell into symmetrical group and were counted if they were large in size, had many mitochondria, and gold labeling. Out of all of the boutons sampled, the BG boutons only made up 0.3%. Of the symmetric synapses, 16.7% were from BG, 6.7% from dTRN and 33.3% from vTRN. The difference in vTRN and dTRN's proportions of BG boutons is notable. This could be due to small sample size, but given that the TRN receives inputs from both the SNr, which projects ventrally, and the GPe, which projects in both dorsal and ventral aspects, it is plausible that there may be more BG boutons ventrally.

The average bouton diameters for the amygdala/SC and BG were 2.14 and 1.80  $\mu\text{m}$ , respectively. It is thought that large boutons with many mitochondria and vesicles may be present with highly active networks and that even a small number of large

boutons could initiate widespread effects (Zikopoulos and Barbas, 2007a). This has been suggested in a few amygdala boutons, as a small percentage of these larger boutons can form multiple synapses with distinct shafts of TRN neurons (Zikopoulos and Barbas, 2012). Thus, it makes sense that amygdala, SC, and BG boutons are not found in abundance across the TRN.

Amygdala, SC, and BG boutons may have also been seen in a higher quantity in the ventral aspect because almost all the primary and secondary dendritic order, 92.86% and 80.43%, respectively, were populated by the ventral dendrites in this analysis, and we have established that larger boutons with more mitochondria tend to form synapses more proximally. Figure 13B confirms and restates this relationship by displaying the relative proportions of each class of boutons across dendritic order. 53.9%, 68.6%, 88.1%, and 89.1% of the boutons on primary, secondary, tertiary, and quaternary branches were from D-terminal boutons. 44.5%, 29.1%, 9.2%, and 8.8% of the boutons on primary, secondary, tertiary, and quaternary branches were from L-terminal boutons. Symmetric bouton percentages stayed relatively consistent across all dendritic orders.

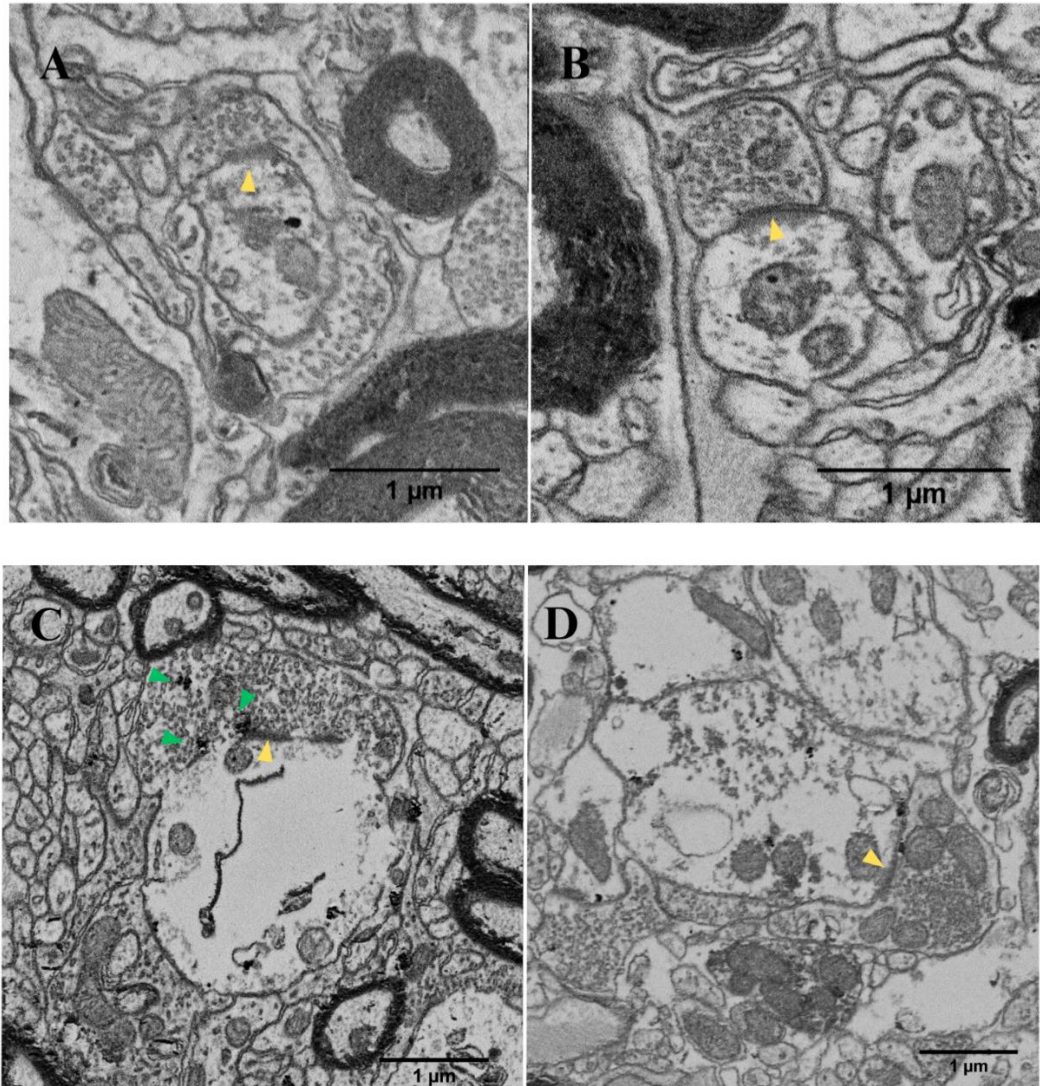
**Figure 14. Relative Abundance of Bouton Classes**

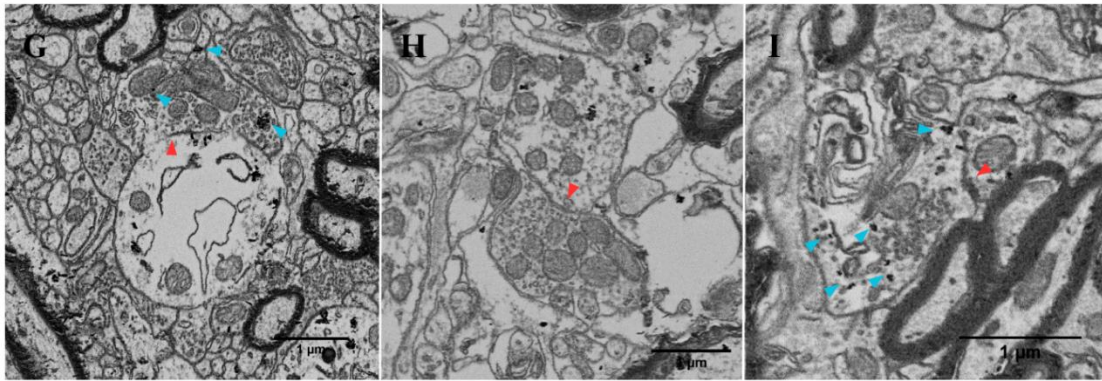
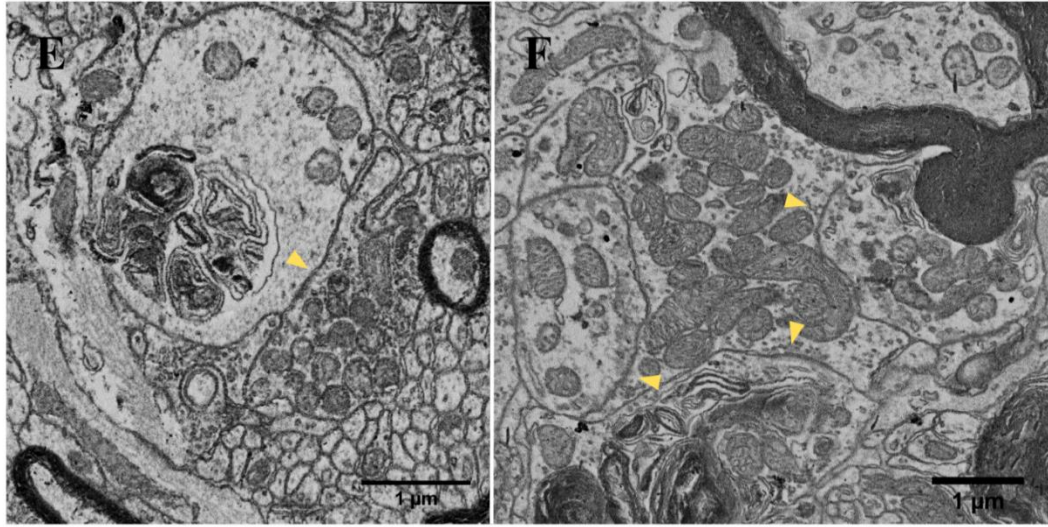


(A) Bar chart displaying percentages of dorsal and ventral dendrites that synapse with different classes of boutons (asymmetric with 0-1 mitochondria, asymmetric with 2+ mitochondria, and symmetric). (B) Bar chart displaying percentages of dendrites from different orders that synapse with different classes of boutons.

The categorizations of D- and L- terminals indicated that boutons from the cortex should have asymmetric PSD and 0-1 mitochondria while boutons from the thalamus should have asymmetric PSD and 2+ mitochondria. Based on these criteria alone, we saw that 73.7% of boutons were from the cortex and 24.2% were from the thalamus across the entire TRN. However, thalamic boutons are immunoreactive to PV which was implemented in case RBR (Zikopoulos and Barbas 2007a). Therefore, we leveraged this immunoreactivity to confirm the features of thalamic boutons compared to that of cortical boutons. Interestingly, all of the boutons that were unlabeled in this case and were presumed to be cortical boutons had expected mitochondrial amounts that ranged between 0-1. However, boutons that demonstrated immunoreactivity to PV, showed overlap with cortical boutons on the premise of their mitochondrial content. Of those that were labeled for PV, 69.2% had the expected 2-4 mitochondria. However, 30.8% only had 0-1 mitochondria, indicating there may be some overlap in these bouton categorizations, suggesting a limitation in the utilization of D-, L-, and F-terminal nomenclature.

**Figure 15.** Electron Microscopy Bouton Categories



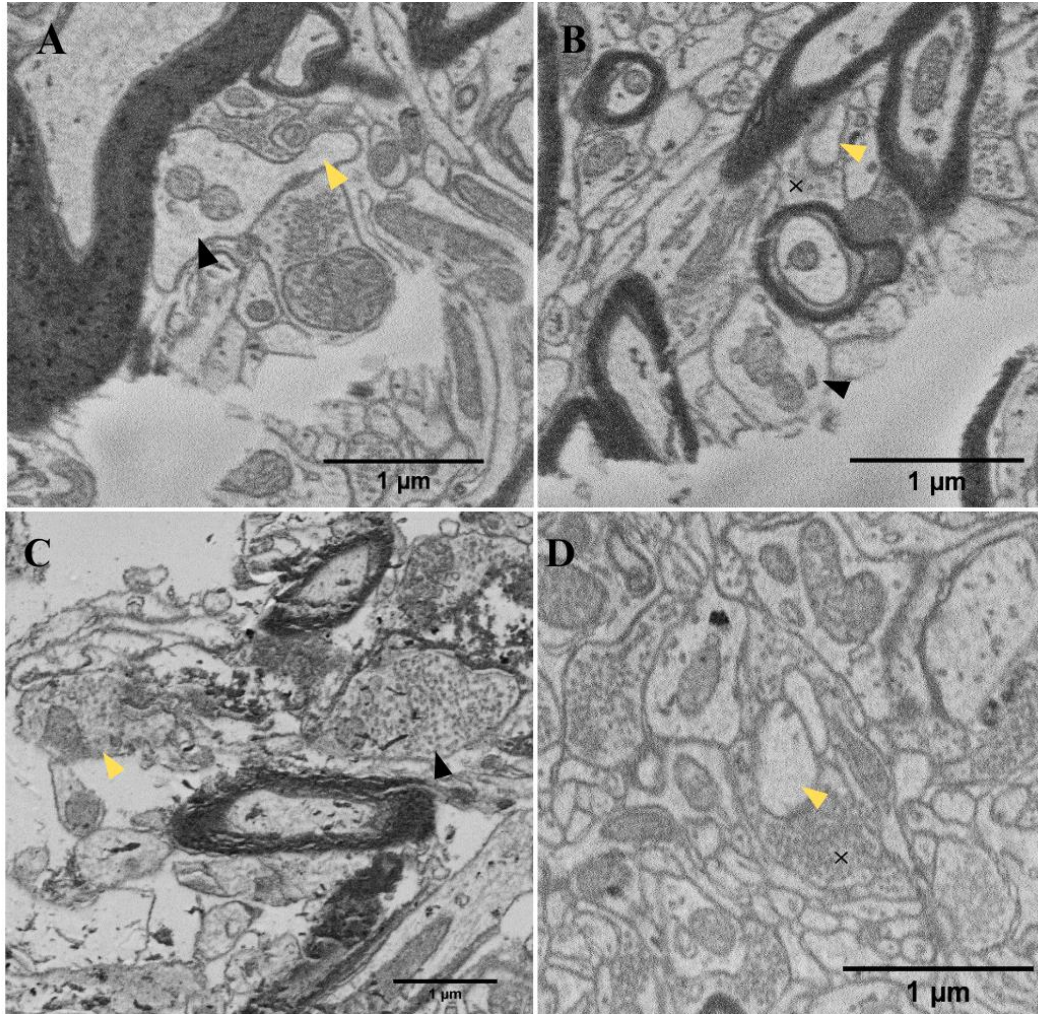


(A) Bouton from cortex as indicated by zero mitochondria, asymmetric PSD (yellow arrow), and many small round vesicles. (B) Bouton from cortex as indicated by one mitochondrion, asymmetric PSD (yellow arrow), and many small round vesicles. (C) Bouton from the thalamus as indicated by asymmetric PSD (yellow arrow) and PV labeling (green arrows). (D-E) vTRN boutons likely to be from SC as indicated by asymmetric PSD (yellow arrow), many mitochondria, and large size. (F) Dorsally located multisynaptic amygdala bouton with asymmetric PSD (yellow arrows), many mitochondria, and large size. (G-H) BG bouton as indicated by symmetric PSD (red arrow), many mitochondria, large size, and labeling by GABA (blue arrows). In H, GABA labeling was seen, but not in the image above. (I) TRN recurrent collateral as indicated by symmetric PSD (red arrow), GABA labeling (blue arrows), and fewer vesicles. The imaged collateral is larger than most that were seen at the EM level.

### 3.5 Filipodia and spines

Of the boutons analyzed, there were a small proportion that synapsed on dendritic thorns. Previous studies have not mentioned an abundant thorn population within the TRN which was reflected in my analysis as well as only ten in the dTRN and two in the vTRN were identified. At the EM level, thorns could present either as dendritic protrusions extending off the main dendritic body or they could appear as dendrites that exist for a portion of the series without mitochondria as shown in Figure 16D. Importantly, any synapses made with dendritic thorns are asymmetric and excitatory (Berry and Nedivi, 2017). Filipodia, which are membrane protrusions important for interaction and development in the brain, were found much more abundantly throughout the TRN (De Biasi et al., 1996; Wit and Hiesinger, 2022). At the EM level, filopodia appeared as small dendritic protrusions extending from a larger dendrite; however, following a few sections, they would disappear. Rare classes were also identified such as filopodia that formed synapses, contained mitochondria, and continued for many sections. Importantly, distinguishing filopodia from thorns at the EM level is difficult. To confirm the relative abundance of thorns and filopodia, tubulin staining should be utilized as it selectively labels filopodia. Most spines and filopodia formed on more distal branches of dendrites matching what has been demonstrated in other species (Lubke, 1993). The vast majority of thorns, for example, were found on tertiary dendrites (75%). They were also seen on secondary (17%) and quaternary dendrites (9%), but importantly, none were seen on primary dendrites.

**Figure 16.** Filopodia and Thorns Visualized by Electron Microscopy



(A) Common filopodia (yellow arrow) on tertiary dendrite (black arrow). (B) Filopodia (yellow arrow) that branched off a tertiary main dendritic body (black arrow) and formed synapse (black X). (C) Filopodia containing mitochondria (yellow arrow) as it branched off secondary main dendritic body (black arrow). (D) Portion of tertiary dendrite without mitochondria indicative of a spine (yellow arrow) that forms synapses (black X).

#### 4. DISCUSSION

There are few studies examining the primate TRN; however, from these, information has been derived about the function, structure, and importance of the nucleus. Core and matrix circuitry has been a recent consideration in examining the TRN that has shifted research perspectives. While it is understood that core circuits are vital for sensory processing and matrix circuits consolidate sensory experiences for the configuration of consciousness, little is known about the relevance of the TRN in this thalamocortical circuitry. Characterizing regions of the TRN divergent in their core and matrix distributions appears to be a good starting point in addressing this gap in knowledge as morphological heterogeneity has been suggested from our analysis.

Examination of the dTRN and vTRN, both with and without the context of dendritic order, served to sample matrix and core sectors. Through such analyses, the heterogeneity of the TRN was evident. Analyzing cellular architecture, it was apparent that most somata were elongated or round with bipolar or multipolar organizations, with limited distinctions between the dTRN and vTRN. As aforementioned, cell shape may have more to do with space limitations rather than for serving a physiological purpose; however, while multipolar cells are prevalent throughout the central nervous system, bipolar neurons tend to be less common. One of the regions they predominate is in the retina of the eye, which is an important afferent to the LGN, positioned in proximity to the vTRN (Schiller, 2010; Sokhadze et al., 2018b). Meanwhile, multipolar cells have numerous dendritic arbors, which may increase the computational power of their

associated neurons and therefore have implications on their efficiency and ability to be involved with complex communication (Dasika et al., 2007). Continuing to examine if there are differences in soma features between the dTRN and vTRN both rostrally and caudally may help to determine additional functional aspects of these TRN sectors.

The dTRN had larger SDs that did not waver significantly when occupied more proximally or distally. Meanwhile the vTRN's SDs were smaller when formed more distally and decreased significantly between the primary and tertiary dendrite. This was further confirmed as the dTRN tertiary SD was higher than that of the vTRN SD. On the basis of bouton size, the dTRN synapses showed a greater reduction in size when on more distal branches compared to proximal as statistically significant decreases were seen across all orders of dendrites, unlike what was seen at the vTRN. This was further established as the dTRN boutons were significantly smaller than the vTRN boutons when examining the secondary and tertiary branches separately. Given that the number of synapses a cell receives is related to its complexity, these distinctions may be relevant to functional aspects of the core and matrix circuits. Furthermore, 97.9% of the TRN synapses were excitatory boutons while only 2.1% were inhibitory, suggesting a specific balance of excitatory and inhibitory boutons synapsing with TRN dendrites (Figure 17). Notably a greater population of amygdala, SC, and BG boutons seen ventrally.

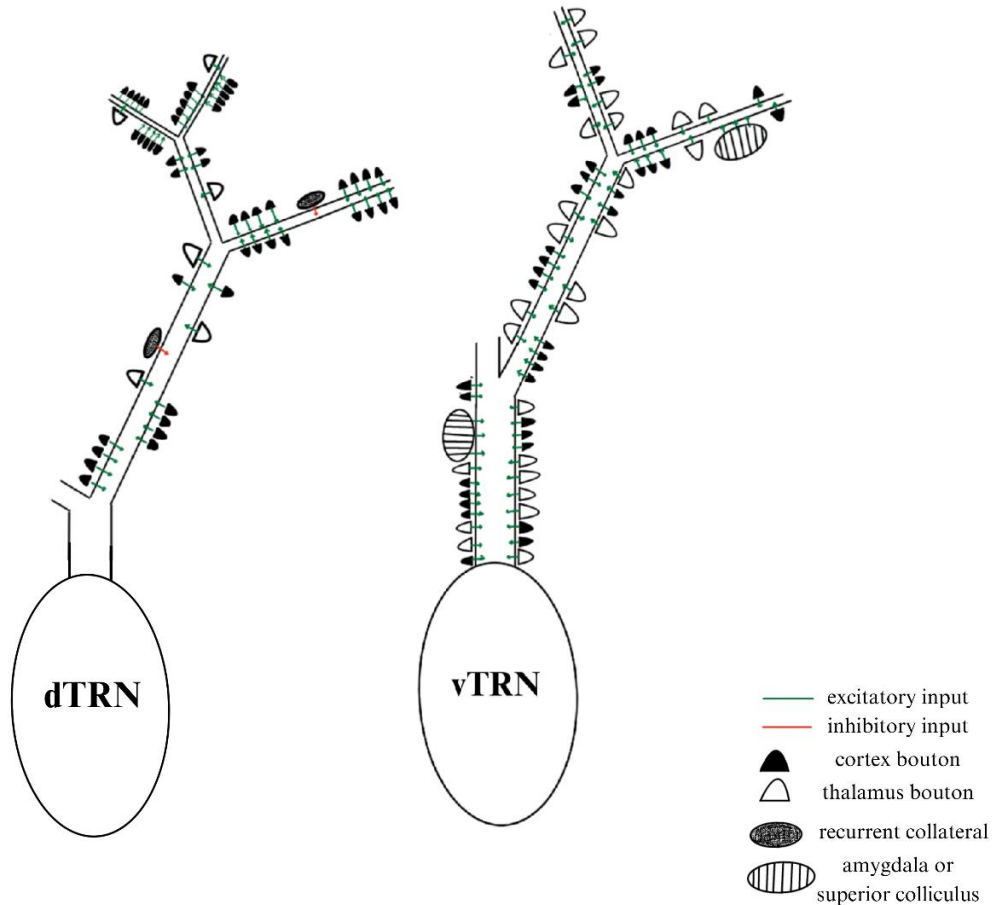
Aside from seeing signs of novel heterogeneity, we also observed trends seen in prior morphological studies, indicating that even in functionally distinct regions, certain foundational aspects of TRN morphology stay intact. These included that small

boutons tend to be round with few mitochondria and synapse more distally while large boutons tend to have more mitochondria and synapse more proximally. We saw that filopodia and thorns formed on branches located distally to the primary dendrite. Furthermore, we were able to categorize analyzed boutons based on D-, L-, and F-terminal classes, for the most part.

While there is limited research on morphological comparisons of core and matrix TRN sectors, it has also not been well-established as to what the role of the TRN was in core and matrix communication. Upon counting and evaluating over 2500 synaptic profiles, it is apparent that afferents to the TRN provide a delicate balance of excitation and are able to effect thalamocortical communication through the TRN. Given that many areas of the brain synapse at the TRN where information is modulated before transmission, it suggests that the TRN's inhibitory action is essential for performing sensory and executive functions. Studying synaptic profiles confirmed this complexity and further supports the TRN's role in selective attention and other cognitive functions.

Disruptions to core-matrix processes have been shown to lead to neurological deficits including but not limited to the inability to shift attention, sensory overactivity, and sleep abnormalities. As anatomy is often directly tied to function, disruption in core-matrix processes may arise at the cellular level. If there are alterations in the balance of excitation and inhibition of inputs to the TRN, for example, the TRN's ability to promote activity in the cortex and perform sensory and executive functions may be reduced. Therefore, creating criteria through quantification of normal morphology in the TRN is vital for understanding disease not just in rhesus macaque but also in humans.

**Figure 17.** Summary of Synapse Distributions



dTRN and vTRN dendrites with ratios of boutons across all dendritic orders. Note that the dTRN and vTRN did not have data from the primary branch and quaternary branch, respectively. Dendritic thickness was drawn to scale; however, dendritic length was not. In the dTRN, 86%, 90%, and 89% of the secondary, tertiary, and quaternary branches received synapses from the cortex with smaller populations of thalamic boutons and recurrent collaterals being present as well. In the vTRN, 54%, 58%, and 53% of the primary, secondary, and tertiary branches received synapses from the cortex. On these same branches, 40%, 37%, and 42% received synapses from the thalamus, with smaller populations of amygdala/SC boutons being present as well. Due to their small population, no boutons from the BG were visualized.

#### 4.1 Limitations and future analyses

While we were able to determine heterogeneity in functionally distinct regions based on core and matrix circuitry, the findings could be strengthened by sampling dendrites across all dendritic orders dorsally and ventrally. Since most of the ventral dendrites analyzed were more proximal while the dorsal dendrites were more distal, it made it difficult to distinguish if differences identified were due to core and matrix characteristics or relative proximity to the cell body. By controlling for dendritic order, we were able to examine differences in the dTRN and vTRN in secondary and tertiary orders of dendrites adequately; however, more data would be needed to do the same examinations in the primary and quaternary orders. Furthermore, there are afferents not included in this analysis that project to the TRN such as those arising from the brainstem and basal forebrain. Due to the wide diversity in projection types from these regions, and the need for understanding the most prevalent synapses, we avoided characterizing the majority of brainstem and basal forebrain structures. However, importantly, some boutons from these regions may be indistinguishable from other classes of boutons that were identified. For instance, the locus coeruleus noradrenergic projections to the TRN were noted to asymmetrically synapse on dendrites covering a wide distribution of sizes (major diameters between 1 and 5  $\mu\text{m}$ ) (Asanuma, 1992). Furthermore, a pathway from the caudal basal forebrain was found to send GABAergic projections to the TRN (Jourdain et al., 1989; Asanuma and Porter, 1990). Synapses of these kind were described to be symmetric, form on larger dendrites, and possess PV immunoreactivity (Jourdain et al., 1989). There was also the potential of overlap of smaller boutons from the amygdala

and SC with cortical or thalamic boutons, as well as overlap between the categories defined for cortical and thalamic boutons, as determined from our analysis. In order to address these limitations, we could implore tracer techniques to accurately identify boutons from different origins and classify their morphological features. Furthermore, at the EM level, we could make use of variations in immunoreactivity of different classes of boutons to further distinguish them in large and representative quantities.

## 5. CONCLUSION

The TRN covers the entire thalamus in primates, eliciting modulatory effects through inhibition of thalamocortical communication. While originally identified as a homogenous structure, the TRN has since been determined to be heterogenous on a functional, topographical, and neurochemical basis. Through leveraging regions of the TRN that differ in their distributions of core and matrix fibers, our study also suggests heterogeneity on an architectural scale. We noted differences in anatomy within the core and matrix TRN sectors at the level of SD, bouton size, and relative proportions of boutons. We also confirmed relationships seen across a variety of morphological studies in literature. It is clear then that the amalgamation of core and matrix circuits in the TRN, with their distinct architectures, are central to the TRN's ability to participate in complex cognitive processes. As anatomy often underlies function, alterations in morphology may cause disruptions to circuitry, resulting in a reduced execution of cognitive functions and the potential formation of neurological abnormalities. Therefore, morphological data in TRN sectors that differ on the basis of their core and matrix circuitry is vital for establishing a cellular-level model that can be applied to understand disease.

## BIBLIOGRAPHY

- Asanuma, C. (1992). Noradrenergic innervation of the thalamic reticular nucleus: a light and electron microscopic immunohistochemical study in rats. *The Journal of Comparative Neurology*, 319(2), 299–311.
- Asanuma, C. (1994). GABAergic and pallidal terminals in the thalamic reticular nucleus of squirrel monkeys. *Experimental Brain Research*, 101(3), 439–451.  
<https://doi.org/10.1007/bf00227337>
- Asanuma, C., & Porter, L. L. (1990). Light and electron microscopic evidence for a GABAergic projection from the caudal basal forebrain to the thalamic reticular nucleus in rats. *The Journal of Comparative Neurology*, 302(1), 159–172.
- Basso, M. A., & May, P. W. (2017). Circuits for Action and Cognition: A View from the Superior Colliculus. *Annual Review of Vision Science*, 3(1), 197–226.
- Berezhnaya, L. A. (2006). Neuronal organization of the reticular nucleus of the thalamus in adult humans. *Neuroscience and Behavioral Physiology*, 36(5), 519–525.
- Berry, K. P., & Nedivi, E. (2017). Spine dynamics: Are they all the same? *Neuron*, 96(1), 43–55.
- Bickford, M. E. (2016). Thalamic Circuit Diversity: Modulation of the Driver/Modulator Framework. *Frontiers in Neural Circuits*, 9, 86.  
<https://doi.org/10.3389/fncir.2015.00086>
- Bird, A. D., & Cuntz, H. (2016). Optimal Current Transfer in Dendrites. *PLoS Computational Biology*, 12(5), e1004897.  
<https://doi.org/10.1371/journal.pcbi.1004897>
- Bragg, E. M., Fairless, E. A., Liu, S., & Briggs, F. (2016). Morphology of visual sector thalamic reticular neurons in the macaque monkey suggests retinotopically specialized, parallel stream-mixed input to the lateral geniculate nucleus. *Journal of Comparative Neurology*, 525(5), 1273–1290.
- Campbell, M. J., & Morrison, J. H. (1989). Monoclonal antibody to neurofilament protein (SMI-32) labels a subpopulation of pyramidal neurons in the human and monkey neocortex. *The Journal of Comparative Neurology*, 282(2), 191–205.
- Contreras-Rodríguez, J. (2003). Neurochemical heterogeneity of the thalamic reticular and perireticular nuclei in developing rabbits: patterns of calbindin expression. *Developmental Brain Research*, 144(2), 211–221.

- Cox, C. L., Huguenard, J. R., & Prince, D. A. (1996). Heterogeneous axonal arborizations of rat thalamic reticular neurons in the ventrobasal nucleus. *The Journal of Comparative Neurology*, 366(3), 416–430.
- Crabtree, J. H. (1996). Organization in the somatosensory sector of the cat's thalamic reticular nucleus. *Journal of Comparative Neurology*, 366(2), 207–222.
- Crabtree, J. H. (1998). Organization in the auditory sector of the cat's thalamic reticular nucleus. *Journal of Comparative Neurology*, 390(2), 167–182.
- Crabtree, J. W. (2018). Functional Diversity of Thalamic Reticular Subnetworks. *Frontiers in Systems Neuroscience*, 12, 41. <https://doi.org/10.3389/fnsys.2018.00041>
- Crick, F. (1984). Function of the thalamic reticular complex: the searchlight hypothesis. *Proceedings of the National Academy of Sciences of the United States of America*, 81(14), 4586–4590.
- Dasika, V. K., White, J. A., & Colburn, H. S. (2007). Simple models show the general advantages of dendrites in coincidence detection. *Journal of Neurophysiology*, 97(5), 3449–3459.
- De Biasi, S., Amadeo, A., Arcelli, P., Frassoni, C., Meroni, A., & Spreafico, R. (1996). Ultrastructural characterization of the postnatal development of the thalamic ventrobasal and reticular nuclei in the rat. *Anatomy and Embryology*, 193(4), 341–353.
- Deleuze, C., & Huguenard, J. R. (2006). Distinct Electrical and Chemical Connectivity Maps in the Thalamic Reticular Nucleus: Potential Roles in Synchronization and Sensation. *Journal of Neuroscience*, 26(33), 8633–8645.
- Gandia, J. A., De Las Heras, S., García, M., & Giménez-Amaya, J. M. (1993). Afferent projections to the reticular thalamic nucleus from the globus pallidus and the substantia nigra in the rat. *Brain Research Bulletin*, 32(4), 351–358.
- García-Cabezas, M. Á., John, Y. J., Barbas, H., & Zikopoulos, B. (2016). Distinction of Neurons, Glia and Endothelial Cells in the Cerebral Cortex: An Algorithm Based on Cytological Features. *Frontiers in Neuroanatomy*, 10, 107.
- Guillery, R. W. (1995). Anatomical evidence concerning the role of the thalamus in corticocortical communication: a brief review. *Journal of Anatomy*, 187(Pt 3), 583–592.

- Guillery, R. W., & Harting, J. K. (2003). Structure and connections of the thalamic reticular nucleus: Advancing views over half a century. *The Journal of Comparative Neurology*, *463*(4), 360–371.
- Hallanger, A. E., Levey, A. I., Lee, H. C., Rye, D. B., & Wainer, B. H. (1987). The origins of cholinergic and other subcortical afferents to the thalamus in the rat. *Journal of Comparative Neurology*, *262*(1), 105–124.
- Hazrati, L.-N., & Parent, A. (1991). Projection from the external pallidum to the reticular thalamic nucleus in the squirrel monkey. *Brain Research*, *550*(1), 142–146.
- Houser, C. R., Vaughn, J. E., Barber, R. P., & Roberts, E. (1980). GABA neurons are the major cell type of the nucleus reticularis thalami. *Brain Research*, *200*(2), 341–354.
- Jiang, Y., Patton, M. H., & Zakharenko, S. S. (2021). A Case for Thalamic Mechanisms of Schizophrenia: Perspective From Modeling 22q11.2 Deletion Syndrome. *Frontiers in Neural Circuits*, *15*, 769969.
- John, Y. J., Zikopoulos, B., Bullock, D., & Barbas, H. (2016). The Emotional Gatekeeper: A Computational Model of Attentional Selection and Suppression through the Pathway from the Amygdala to the Inhibitory Thalamic Reticular Nucleus. *PLoS Computational Biology*, *12*(2), e1004722.
- Jones, E. G. (1985). *The Thalamus*. New York: Plenum.
- Jones, E. G. (1975). Some aspects of the organization of the thalamic reticular complex. *The Journal of Comparative Neurology*, *162*(3), 285–308.
- Jones, E. G. (1998). Viewpoint: the core and matrix of thalamic organization. *Neuroscience*, *85*(2), 331–345.
- Jourdain, A., Semba, K., & Fibiger, H. C. (1989). Basal forebrain and mesopontine tegmental projections to the reticular thalamic nucleus: an axonal collateralization and immunohistochemical study in the rat. *Brain Research*, *505*(1), 55–65.
- Joyce, M. K. P., & Barbas, H. (2018). Cortical Connections Position Primate Area 25 as a Keystone for Interoception, Emotion, and Memory. *The Journal of Neuroscience*, *38*(7), 1677–1698.
- Kong, Q.-M., Qiao, H., Liu, C.-Z., Zhang, P., Li, K., Wang, L., Li, J.-T., Su, Y., Li, K.-Q., Yan, C.-G., Mitchell, P. B., & Si, T.-M. (2018). Aberrant intrinsic functional connectivity in thalamo-cortical networks in major depressive disorder. *CNS Neuroscience & Therapeutics*, *24*(11), 1063–1072.

- Krauzlis, R. J., Lovejoy, L. P., & Zénon, A. (2013). Superior Colliculus and Visual Spatial Attention. *Annual Review of Neuroscience*, 36(1), 165–182.
- Kultas-Ilinsky, K., Ilinsky, I., Warton, S., & Smith, K. R. (1983). Fine structure of nigral and pallidal afferents in the thalamus: an EM autoradiography study in the cat. *The Journal of Comparative Neurology*, 216(4), 390–405.
- Kultas-Ilinsky, K., Reising, L., Yi, H., & Ilinsky, I. A. (1997). Pallidal afferent territory of the *Macaca mulatta* thalamus: neuronal and synaptic organization of the VAdc. *The Journal of Comparative Neurology*, 386(4), 573–600.
- Lanciego, J. L., Luquin, N., & Obeso, J. A. (2012). Functional neuroanatomy of the basal ganglia. *Cold Spring Harbor Perspectives in Medicine*, 2(12), a009621–a009621.
- Lee, S.-H., Govindaiah, G., & Cox, C. L. (2007). Heterogeneity of firing properties among rat thalamic reticular nucleus neurons. *The Journal of Physiology*, 582(1), 195–208.
- Levey, A. I., Hallanger, A. E., & Wainer, B. H. (1987). Cholinergic nucleus basalis neurons may influence the cortex via the thalamus. *Neuroscience Letters*, 74(1), 7–13.
- Liu, X. B., & Jones, E. G. (1999). Predominance of corticothalamic synaptic inputs to thalamic reticular nucleus neurons in the rat. *The Journal of Comparative Neurology*, 414(1), 67–79.
- Llinás, R. R., & Steriade, M. (2006). Bursting of Thalamic Neurons and States of Vigilance. *Journal of Neurophysiology*, 95(6), 3297–3308.
- Lübke, J. (1993). Morphology of neurons in the thalamic reticular nucleus (TRN) of mammals as revealed by intracellular injections into fixed brain slices. *Journal of Comparative Neurology*, 329(4), 458–471.
- Marks, G. A., & Roffwarg, H. P. (1993). Spontaneous activity in the thalamic reticular nucleus during the sleep/wake cycle of the freely-moving rat. *Brain Research*, 623(2), 241–248.
- Münkle, M. C., Waldvogel, H. J., & Faull, R. L. M. (2000). The distribution of calbindin, calretinin and parvalbumin immunoreactivity in the human thalamus. *Journal of Chemical Neuroanatomy*, 19(3), 155–173.
- Ohara, P. T. (1988). Synaptic organization of the thalamic reticular nucleus. *Journal of Electron Microscopy Technique*, 10(3), 283–292.

- Ohara, P. T., & Havton, L. A. (1996). Dendritic arbors of neurons from different regions of the rat thalamic reticular nucleus share a similar orientation. *Brain Research*, 731(1-2), 236–240.
- Ohara, P. T., & Lieberman, A. R. (1985). The thalamic reticular nucleus of the adult rat: experimental anatomical studies. *Journal of Neurocytology*, 14(3), 365–411.
- Ouda, L., Druga, R., & Syka, J. (2011). Distribution of SMI-32-immunoreactive neurons in the central auditory system of the rat. *Brain Structure and Function*, 217(1), 19–36.
- Ouhaz, Z., Fleming, H., & Mitchell, A. S. (2018). Cognitive Functions and Neurodevelopmental Disorders Involving the Prefrontal Cortex and Mediodorsal Thalamus. *Frontiers in Neuroscience*, 12, 33. <https://doi.org/10.3389/fnins.2018.00033>
- Partlow, G. D., Colonnier, M., & Szabo, J. (1977). Thalamic projections of the superior colliculus in the rhesus monkey, *Macaca mulatta*. A light and electron microscopic study. *The Journal of Comparative Neurology*, 72(3), 285–318.
- Paxinos, G., Huang, X. F., & Toga, A. W. (2000). *The rhesus monkey brain in stereotaxic coordinates*. San Diego, CA: Academic Press.
- Peters, A., Palay, S. L., & Webster, H. deF. (1991). *The Fine Structure of the Nervous System*. Oxford University Press, USA.
- Pinault, D. (2004). The thalamic reticular nucleus: structure, function and concept. *Brain Research Reviews*, 46(1), 1–31.
- Pinault, D., Smith, Y., & Deschênes, M. (1997). Dendrodendritic and Axoaxonic Synapses in the Thalamic Reticular Nucleus of the Adult Rat. *The Journal of Neuroscience*, 17(9), 3215–3233.
- Rodríguez, J. M., Noristani, H. N., Hoover, W. B., Linley, S. B., & Vertes, R. P. (2011). Serotonergic projections and serotonin receptor expression in the reticular nucleus of the thalamus in the rat. *Synapse*, 65(9), 919–928.
- Schiller, P. H. (2010). Parallel information processing channels created in the retina. *Proceedings of the National Academy of Sciences of the United States of America*, 107(40), 17087–17094.
- Serrano, M. E., Kim, E., Petrinovic, M. M., Turkheimer, F., & Cash, D. (2022). Imaging Synaptic Density: The Next Holy Grail of Neuroscience? *Frontiers in Neuroscience*, 16, 796129. <https://doi.org/10.3389/fnins.2022.796129>

- Sherman, S. M., & Guillery, R. W. (2002). The role of the thalamus in the flow of information to the cortex. *Philosophical Transactions of the Royal Society of London. Series B: Biological Sciences*, 357(1428), 1695–1708.
- Sokhadze, G., Campbell, P. W., & Guido, W. (2018a). Postnatal development of cholinergic input to the thalamic reticular nucleus of the mouse. *European Journal of Neuroscience*, 49(8), 978–989.
- Sokhadze, G., Seabrook, T. A., & Guido, W. (2018b). The absence of retinal input disrupts the development of cholinergic brainstem projections in the mouse dorsal lateral geniculate nucleus. *Neural Development*, 13(1), 27.  
<https://doi.org/10.1186/s13064-018-0124-7>
- Son, J. (2022). *Core and matrix innervation of thalamic reticular nucleus in primates*. M.S. thesis – Boston University. <https://open.bu.edu/handle/2144/44473>
- Spreafico, R., Battaglia, G., & Frassoni, C. (1991). The reticular thalamic nucleus (RTN) of the rat: Cytoarchitectural, Golgi, immunocytochemical, and horseradish peroxidase study. *Journal of Comparative Neurology*, 304(3), 478–490.
- Spreafico, R., de Curtis, M., Frassoni, C., & Avanzini, G. (1988). Electrophysiological characteristics of morphologically identified reticular thalamic neurons from rat slices. *Neuroscience*, 27(2), 629–638.
- Timbie, C., García-Cabezas, M. Á., Zikopoulos, B., & Barbas, H. (2020). Organization of primate amygdalar–thalamic pathways for emotions. *PLoS Biology*, 18(2), e3000639.
- Trutzer, I. M., García-Cabezas, M. Á., & Zikopoulos, B. (2019). Postnatal development and maturation of layer 1 in the lateral prefrontal cortex and its disruption in autism. *Acta Neuropathologica Communications*, 7(1), 40.
- Tsumori, T., Yokota, S., Ono, K., & Yasui, Y. (2002). Synaptic organization of GABAergic projections from the substantia nigra pars reticulata and the reticular thalamic nucleus to the parafascicular thalamic nucleus in the rat. *Brain Research*, 957(2), 231–241.
- Wanaverbecq, N., Bodor, Á. L., Bokor, H., Slézia, A., Lüthi, A., & László Acsády. (2008). Contrasting the Functional Properties of GABAergic Axon Terminals with Single and Multiple Synapses in the Thalamus. *The Journal of Neuroscience*, 28(46), 11848–11861.
- Wang, J., & Barbas, H. (2018). Specificity of Primate Amygdalar Pathways to Hippocampus. *The Journal of Neuroscience*, 38(47), 10019–10041.

- Wang, J., John, Y., & Barbas, H. (2021). Pathways for Contextual Memory: The Primate Hippocampal Pathway to Anterior Cingulate Cortex. *Cerebral Cortex*, *31*(3), 1807–1826.
- Weyand, T. G. (2016). The multifunctional lateral geniculate nucleus. *Reviews in the Neurosciences*, *27*(2), 135–157. <https://doi.org/10.1515/revneuro-2015-0018>
- Williamson, A. M., Ohara, P. T., & Ralston, H. J. (1993). Electron microscopic evidence that cortical terminals make direct contact onto cells of the thalamic reticular nucleus in the monkey. *Brain Research*, *631*(1), 175–179.
- Wilt, B. A., Burns, L. D., Wei Ho, E. T., Ghosh, K. K., Mukamel, E. A., & Schnitzer, M. J. (2009). Advances in Light Microscopy for Neuroscience. *Annual Review of Neuroscience*, *32*(1), 435–506.
- Wit, C. B., & Hiesinger, P. R. (2022). Neuronal filopodia: From stochastic dynamics to robustness of brain morphogenesis. *Seminars in Cell & Developmental Biology*, *133*, 10–19.
- Zikopoulos, B., & Barbas, H. (2006). Prefrontal Projections to the Thalamic Reticular Nucleus form a Unique Circuit for Attentional Mechanisms. *Journal of Neuroscience*, *26*(28), 7348–7361.
- Zikopoulos, B., & Barbas, H. (2007a). Circuits for Multisensory Integration and Attentional Modulation Through the Prefrontal Cortex and the Thalamic Reticular Nucleus in Primates. *Reviews in the Neurosciences*, *18*(6), 417–438. <https://doi.org/10.1515%2Frevneuro.2007.18.6.417>
- Zikopoulos, B., & Barbas, H. (2007b). Parallel Driving and Modulatory Pathways Link the Prefrontal Cortex and Thalamus. *PLoS ONE*, *2*(9), e848.
- Zikopoulos, B., & Barbas, H. (2012). Pathways for Emotions and Attention Converge on the Thalamic Reticular Nucleus in Primates. *Journal of Neuroscience*, *32*(15), 5338–5350.
- Zikopoulos, B., & Barbas, H. (2013). Altered neural connectivity in excitatory and inhibitory cortical circuits in autism. *Frontiers in Human Neuroscience*, *7*, 609.

## CURRICULUM VITAE

